Second Order

Abel Inversion with Allowance for the Spatial Resolution

P. Smeulders

IPP 2/240 August 1978

MAX-PLANCK-INSTITUT FÜR PLASMAPHYSIK

8046 GARCHING BEI MÜNCHEN

MAX-PLANCK-INSTITUT FÜR PLASMAPHYSIK

GARCHING BEI MÜNCHEN

Second Order

Abel Inversion with Allowance for the Spatial Resolution

P. Smeulders

IPP 2/240 August 1978

Die nachstehende Arbeit wurde im Rahmen des Vertrages zwischen dem Max-Planck-Institut für Plasmaphysik und der Europäischen Atomgemeinschaft über die Zusammenarbeit auf dem Gebiete der Plasmaphysik durchgeführt.

Second Order
Abel Inversion with Allowance for the
Spatial Resolution.

P. Smeulders

IPP 2/240
August 1978

Abstract

A new Abel inversion method is presented. Allowance for the second order expansion over a given spatial interval (piecewise fit) and allowance for the spatial resolution inherent in the detector system is made.

A comparison is made with a previous method due to Gorenflo [1] using test functions. A significant improvement is found. The degree of smoothness of the raw data prior to the Abel inversion can be obtained.

Contents

1. Introduction

In line of sight measurements where Abel inversion must be carried out allowance is not usually made for the finite spatial resolution (i.e. the "beam" width). This is sometimes overcome by having a narrow beam of sight at the cost of highly wanted flux but it is often simply neglected reducing the significance of the measurement. By taking into account the complete geometry of the "optics" and including the second order expansion the region of validity of the Abel inversion is greatly extended.

2. The Abel-Integral

The usual well-known Abel-integral is [1 1]

$$G(t) = \int_0^t (t-s)^{-1/2}\, g(s)\, ds, \quad 0 \leqslant s \leqslant 1, \; 0 \leqslant t \leqslant 1, \; G(0) = 0 \qquad (1)$$

Here g (s) can be, for example, the local emissivity and G(t) is the line integrated emission or the measured flux as a function of the radial position. The problems connected with the inversion of (1) are well known. Three possible numerical solutions are given by Gorenflo [1 1].

If very steep gradients are present (the soft X-ray emission from hot plasmas for example) or if the spatial resolution is not sufficiently good, these more simple methods will break down.

A more complete treatment of the problem is necessary, in which steeper gradients and a limited spatial resolution are taken into account.

3. The Flux Integral

In order to calculate the flux integral one has to start with the detector geometry. This geometry is given by the area of the detector together with beam stops. These define the plasma volume that illuminates the detector. (Hatched area in Fig.1).

The calculations presented here are based on a geometry consisting of two slit beam stops S_1 and S_2 . The slits are orientated such that the plasma can be assumed homogeneous along the slit direction. In principle, the final computer code could be slightly modified for any detector configuration, however the assumption of the axial plasma symmetry is always necessary. Also apart from the axial symmetry the usual azimuthal symmetry is assumed. In praxis, however, local azimuthal asymmetries may give rise to errors in the Abel inversion.

If ψ is the parameter, which determines the circular magnetic surface, then the flux falling upon the detector is given by

$$\Phi(\psi) = \int_{S_1}\int_{S_2}\int_{\psi'}^{\psi_a} \frac{g(\psi'')}{\sqrt{\psi''-\psi'}}\, d\psi''\, d s_2\, d s_1 \qquad (2)$$

with $\psi = r^2$ and $g(\psi'')$ is the emissivity at the magnetic surface ψ'' (Fig.2). For the particular case, shown in Fig.2, there is a movable slit S_1 together with a fixed slit S_2.

The flux falling on S_1 is then

$$\Phi(\psi) = \int_0^{d_1}\int_0^{d_2}\int_{\psi'}^{\psi_a} \frac{g(\psi'')d\psi''\, \cos^3\alpha\, \cos(\alpha-\vartheta)\, ds_2\, ds_1}{\sqrt{\psi''^2-\psi'^2}\,\left(z_{12}+(d_2/2-s_2)\sin\vartheta\right)^2} \qquad (3)$$

where α is given by

$$Ag(\alpha) = \frac{d_1/2 - s_1 - (d_2/2-s_2)\cos\vartheta}{z_{12} + (d_2/2-s_2)\sin\vartheta} \qquad (4)$$

ϑ is defined by the geometry of the beam stops.

$$\psi' = \frac{l^2(m-1)^2}{2(m^2+1)} \qquad \text{where} \qquad (5)$$

$$m = \operatorname{tg}(\vartheta-\alpha) \qquad (6)$$

With any test function $g(\psi)$ it is now possible to calculate accurately the flux falling upon the detector.

4. The Abel Inversion - Method A of Gorenflo

As indicated by Gorenflo [11], the method A is, in most cases, the most accurate of the three solutions he discusses. Therefore, it is appropriate to compare this method with the new method presented in this paper.

We briefly review this method A of Gorenflo (hencefore referred to as Gorenflo-A). Flux measurements at equally spaced radial position are taken:

$$r_i = (j-1)\,h = (j-1)\,a/N\,;\quad j = 1, N$$

such that

$$F(x_n) = 2\int_{x_n}^{a} \frac{f(r)\,r\,dr}{\sqrt{r^2 - x_n^2}} \simeq 2\sum_{i=n}^{N} f_i \int_{x_i}^{x_{i+1}} \frac{r\,dr}{\sqrt{h^2 - x_n^2}} \qquad (7)$$

with $f_i = f(r_i + h/2)$, a zero order expansion over the interval r_i and r_{i+1}. Therefore we can write

$$F_n = F(x_n) = \sum_{i=n}^{N} \alpha(n,i)\, f_i \;;\quad n = 1, \ldots N \qquad (8)$$

The $\alpha(n,i)$'s form a triangular matrix, which is simple to invert.
Each $\alpha(n,i)$ is in fact twice the length of the section of chord between $r = r_i$ and r_{i+1} as shown in Fig.3.

The new approach presented here has many similarities of the Gorenflo-A method.

5. The Extended Abel Inversion

The Abel inversion routine proposed in this paper is a two-way extension of Gorenflo-A method. Firstly, the intensity function $f(r)$ is expanded to second order over the interval (r_i, r_{i+1}). Note, that for each interval there is a separate expansion. Secondly, the spatial integral is extended over the width of the chord in the plasma defined by the beam stops.

The flux as function of r_n : $F(r_n) = F_n$ can then be written:

$$F_n = \int_0^{d_1}\int_0^{d_2}\int_{r_n}^{a} \frac{f(r'')\, r''\, dr''}{\sqrt{r''^2 - r'^2}}\, A\, ds_2\, ds_1 \; ; \; n = 1, \ldots N \tag{9}$$

$$A = \frac{\cos^3\alpha \cdot \cos(\alpha - \theta)}{(z_{12} + (d_2/2 - s_2)\cdot \sin\theta)^2} \quad \text{and} \quad r' = \sqrt{\psi'}$$

We expand $f(r) = f(b) + f'(b)(r-b) + f''(b)(r-b)^2/2$ with $b = (r_i + r_{i+1})/2$ and $i = 1, N$; $r_{N+1} = a$. This can be written

for $1 < i < N$ as

$$\begin{aligned} f(r) = {} & (-f_{i-1} + 6 f_i + 3 f_{i+1}) \cdot \frac{1}{8} \\ & + (-f_i + f_{i+1}) \cdot \frac{(r-b)}{h} \\ & + (f_{i-1} - 2 f_i + f_{i+1}) \cdot \frac{(r-b)^2}{2h^2} \; ; \; h = a/N \end{aligned} \tag{10}$$

for $i = 1$

$$\begin{aligned} f(r) = {} & (6 f_i + 2 f_{i+1}) \cdot \frac{1}{8} \\ & + (-f_i + f_{i+1}) \cdot \frac{(r-b)}{h} \\ & + (-2 f_i + 2 f_{i+1}) \cdot \frac{(r-b)^2}{2h^2} \end{aligned} \tag{11}$$

and for $i = N$

$$\begin{aligned} f(r) = {} & (3 f_{i-2} - 10 f_{i-1} + 15 f_i) \cdot \frac{1}{8} \\ & + (f_{i-2} - 3 f_{i-1} + 2 f_i) \cdot \frac{(r-b)}{h} \\ & + (f_{i-2} - 2 f_{i-1} + f_i) \cdot \frac{(r-b)^2}{2h^2} \end{aligned} \tag{12}$$

The f_i are the unknown emissivities at $r = r_i$. These are constants, which can be taken outside the integrals.

With aid of expressions (10), (11) and (12) we can write (9) as

$$
\begin{aligned}
F_n = \sum_{i=n}^{N-1} & (-f_{i-1} + 6 f_i + 3 f_{i+1})\, T_1(n,i) \\
& + (-f_i + f_{i+1})\, T_2(n,i) \\
& + (f_{i-1} - 2 f_i + f_{i+1})\, T_3(n,i) \\
& + (3 f_{N-2} - 10 f_{N-1} + 15 f_N)\, T_1(n,N) \\
& + (f_{N-2} - 3 f_{N-1} + 2 f_N)\, T_2(n,N) \\
& + (f_{N-2} - 2 f_{N-1} + f_N)\, T_3(n,N)
\end{aligned}
\qquad (13)
$$

For $n = 1$ the f_{i-1} terms become f_{i+1} in expression (13).

The $T_j(n,i)$ are:

$$T_1(n,i) = \frac{1}{8} \int_0^{d_1} \int_0^{d_2} \int_{r_i}^{r_{i+1}} \frac{r''}{\sqrt{r''^2 - r'^2}}\, dr''\, A\, ds_2\, ds_1 \qquad (14)$$

$$T_2(n,i) = \frac{1}{h} \int_0^{d_1} \int_0^{d_2} \int_{r_i}^{r_{i+1}} \frac{r''(r''-b)}{\sqrt{r''^2 - r'^2}}\, dr''\, A\, ds_2\, ds_1 \qquad (15)$$

$$T_3(n,i) = \frac{1}{2h^2} \int_0^{d_1} \int_0^{d_2} \int_{r_i}^{r_{i+1}} \frac{r''(r''-b)^2}{\sqrt{r''^2 - r'^2}}\, dr''\, A\, ds_2\, ds_1 \qquad (16)$$

After some reorganization we can write the fluxes at $r = r_n$ as:

$F_n = \sum_{i=m}^{N} A(n,i)\, f_i$, where m is defined by the spatial resolution.

For example: in case of an infinitly good spatial resolution $m = n-1$ for $n > 1$, and $m = 1$ for $n = 1$.

The matrix elements $A(n,i)$ are constructed from $T_j(n,i)$ in the following way for $m + 1 < i < N$

$$
\begin{aligned}
A(n,i) &= 3 T_1(n,i-1) + T_2(n,i-1) + T_3(n,i-1) \\
&\quad + 6 T_1(n,i) + T_2(n,i) - 2 T_3(n,i) \\
&\quad - T_1(n,i+1) + T_3(n,i+1) \\
A(n,m) &= - T_1(n,m+1) + T_3(n,m+1) \qquad (17) \\
A(n,m+1) &= 6 T_1(n,m+1) - T_2(n,m+1) - 2 T_3(n,m+1) + \\
&\quad - T_1(n,m+2) + T_3(n,m+2) \\
A(n,N) &= 3 T_1(n,N-1) + T_2(n,N-1) + T_3(n,N-1) + \\
&\quad + 15 T_1(n,N) + 2 T_2(n,N) + T_3(n,N)
\end{aligned}
$$

For $i = 2$ in case of $m = 1$ we have the additional terms:

$$A(n,2) = A(n,2) - T_1(n,1) + T_3(n,1) \qquad (18)$$

And in all cases for $i = N-2$ and $N-1$ we get the additional terms

$$\begin{aligned} A(n,N-2) &= A(n,N-2) + 3\,T_1(n,N) + T_2(n,N) + T_3(n,N) \\ A(n,N-1) &= A(n,N-1) - 9\,T_1(n,N) - 3\,T_2(n,N) - 3\,T_3(n,N) \end{aligned} \qquad (19)$$

Fig.4 illustrates the term $T_1(n,i)$ in a similar way to Fig.3 for the terms: $\alpha(n,i)$ in Gorenflo-A. The hatched area corresponds to eight times the term $T_1(n,i)$. For the situation shown in Fig.4 the values of n and i are: $n = 6$ and $i = 7$. Thus, the value of m for this case would be $m = 2$.

It should be noted that, in the case presented, the integration over the segment (r_i, r_{i+1}) is made by taking a parabolic fit for f_{i-1}, f_i and f_{i+1} (the left hand fit). It is also possible to take f_i, f_{i+1} and f_{i+2} (the right hand fit), which leads to only minor differences for the case of bell shaped intensity profiles. However, the left hand fit does give more accurate results for hollow radial profiles.

In the computer code a choice between the left and right hand fit or their average can be made.

6. The Bell-Shaped Radial Profiles - Ideal Spatial Resolution

The improvement of the extended Abel inversion over the Gorenflo-A method will be shown. The intensity radial profiles of the form

$$f(r) = \frac{1}{1 + (\frac{r}{r_2})^{\alpha}} \qquad (20)$$

are taken. These radial profiles are often a good fit to experimental radial profiles. Thus lending more significance to the conclusions drawn from the comparison made below. In order to distinguish the two newly introduced effects in the Abel inversion, we firstly show the influence of the second order expansion.

The effect of the integration over the volume seen by the detector will be shown in section 7. For an ideal infinite spatial resolution figures 5 to 10 show the differences between Gorenflo-A and the second order expansion method for several different profiles,

as marked in each figure. The radial profiles of the line integrated intensity, the intensity,and the errors for both Abel inversions are indicated. The error is a relative error and is the difference between the test function and the Abel inverted calculated flux divided by the test function. The flux is normalized to that of a detector system with two stops of area 1 cm^2 and 1 cm apart.

It can be seen that for small gradients (Fig.6) both methods yield a good Abel inversion, but for steep gradients (α= 16) only the second order Abel inversion produces a good profile (Fig.16). The average between left and right hand fit for the extended Abel inversion matrix has been used. More than 15 points are needed in order to obtain a correct Abel inversion for steep gradients (α = 16). In the example given here 21 points have been used.

7. Bell-Shaped Radial Profiles - Finite Spatial Resolution

The Abel inversion matrix is calculated for a system of finite size stops. Also for the same system of stops the flux integrals at different radial positions are computed. In this way the radial profile of the flux is obtained. Neglecting the finite spatial resolution, Gorenflo-A is used for an Abel inversion together with the extended Abel version. The latter of course including the dependence on the finite spatial resolution.

Again the Abel inversion matrix is taken to be 21 x 21 points and calculated in double precision. The width of the plasma volume on the median plane seen by the detector system is varied from Δ = o up to 4 cm. The two light stops are of equal width and variable size, 10 cm apart; and the second stop is positioned 15 cm from the plasma centre. The plasma radius is fixed at 11 cm. As in the previous section the flux is normalized for a detector system of unity dimension.

Fig.11 shows the variation of $\bar{\Phi}(r)$ for various spatial resolutions. As can be seen from this figure the influence of the spatial resolution on the flux in the central part of the plasma ($r \leq 6$ cm) is rather small ($\leq 15\,\%$). Thus, when using Gorenflo-A for Abel inversion with a bad spatial resolution (Δ = 4 cm), one still gets a good agreement with the test function in the central part of the profile. However, in the wings the error becomes substantial and is increasing with decreasing spatial

resolution. In addition, the errors due to the flux measurements and multiplied by some factor by the Abel inversion, are masked if one uses the Gorenflo-A Abel inversion routine to handle badly spatial resolved radial profiles. (This will be treated later in section 10). It should be noted that, of course, Gorenflo-A was only developed to handle radial profiles with very good spatial resolution.

Again for very steep profiles ($\alpha = 16$) Figs. 12 and 13 show the relative deviation from the original test function of the Abel inverted flux. Fig. 12 is due to the Gorenflo-A routine and Fig. 13 is due to the extended Abel inversion; both for a spatial resolution of $\Delta = 3$ cm. As can be seen from the figures Gorenflo-A causes a smooth buth large deviation, with a maximum at $r = 7.5$ cm of 70%. The extended Abel inversion has a maximal systematic deviation at $r = 8$ cm of 3%! In addition to this there is an oscillating deviation, which grows towards the outside and is about 3.5% at 9.5 cm . The cause of this oscillation is not precisely known, but is believed to be a numerical problem at the plasma edge, that propagates inwards and which increases with decreasing spatial resolution.

Fig. 14 shows the following as a function of Δ (the spatial resolution):

- the smooth maximal systematic error due to Gorenflo-A (upper trace)
- the oscillating error due to the extended Abel inversion (middle and dotted trace)
- the maximal systematic error due to the latter Abel inversion method (lower trace)

It should be noted, that these three errors are all very much dependent on the type of profile, and especially on the steepness (α). For $\alpha = 4$ for example all three errors are strongly reduced as shown in Fig. 15.

8. Hollow Radial Profiles - Ideal Spatial Resolution

Hollow radial profiles are especially vulnerable to misinterpretation due to errors inherent in the Abel inversion technique. Thus, they serve as good test criteria for Abel inversion routines. Again we take a test function, integrate this function along the chord length. Then, both Abel inversion routines are applied to the calculated flux and the calculated radial profiles compared with the original test function. We have taken a deviation of the function used for the bell-shaped radial profiles, i.e.

$$I(r) = \frac{1}{1 + \left(\frac{r}{r_2 + \delta}\right)^{\alpha}} - \frac{1 - I_o}{1 + \left(\frac{r}{r_2 - \delta}\right)^{\alpha}} \qquad (21)$$

An example is given in Fig.16 on a semi-log scale for $I_o = .0001$, $r_2 = 6$ cm, $\delta = .5$ cm and $\alpha = 16$. Using various parameters the radial profiles of the line emission in plasmas can be simulated. The lower hatched line in Fig.17 is a linear representation of the same function. As can be seen, the radial character of the function is very similar as that observed in real experiments with spectroscopic measurements. Therefore, we will study the problems of the Abel inversion by means of this function.

The parameter I_o is especially important for the accuracy of the Abel inversion in the centre of the plasma. Fig.18 shows the systematic errors of the Gorenflo-A Abel inversion method for ideal spatial resolution as a function of parameter I_o. The value of the intensity in the wings is more or less independent of the parameter I_o and it can be seen that the error in the wings is constant and about 17%. However, it has been found that the systematic overestimation of the Abel inverted flux becomes substantial for lower values of I_o and that the Abel inverted central value saturates to a constant value (Fig.19). This saturated value is dependent on the number of points used for the inversion (Fig.20). An approximate extrapolation of Fig.20 indicates that an uncomfortably high number of points is needed for an accurate Abel inversion with Gorenflo-A for the case of $I(o) = 10^{-4}$.

Since the difference in the central flux is only 0.5%, when decreasing I(o) from 10^{-3} to 10^{-4}, it is practically impossible to distinguish the Abel inverted flux profiles (curve c of Fig.17). But even when I(o) = 10^{-3} the systematic error for Gorenflo-A is still substantial (around a factor of 2).

The extended Abel inversion routine shows much improved characteristics regarding the inversion of hollow profiles (Fig.21). Typically, with Gorenflo-A, the errors in the centre are a factor of 30 and in the wings a factor of 5 larger than with the extended Abel inversion routine. Thus, even when the minimum measurable central intensity is of the order of 10^{-3}, the errors due to this Abel inversion remain acceptable over the complete cross section.

9. Hollow Radial Profiles - Finite Spatial Resolution

In the previous section we have seen the dependence of the accuracy of the Abel inversion routines on the central value of the local intensity I(o). If one can measure the radial flux profile with sufficient precision (.5%), it would be possible to determine the central value of the intensity by Abel inversion down to values of 10^{-3} or less. Values of $I(o) = 10^{-3}$ will thus be used to provide a comparison between the Gorenflo-A and the extended Abel inversion methods with finite spatial resolution.

In Fig.22 is given the systematic error by the Gorenflo-A method for various radial positions as a function of the full spatial resolution Δ. At the radial position (r = 3.5 cm) with the steepest gradient in the test function ($I(o) = 10^{-3}$ and $\alpha = 16$) the error is obviously largest and increases (curve b) with decreasing spatial resolution (increasing Δ). There the Abel inverted radial profile is about a factor of 8 larger than the original test function. The error at the edge (r = 8 cm) also increases with decreasing resolution, although, the error in the centre is not much affected in this particular example.

The behaviour of the extended Abel inversion method, including the dependence of the spatial resolution, is shown in Fig.23 as a function of Δ. The total error is again split into an oscillating and a systematic error. As can be seen from the figure the systematic error is not very dependent of the spatial resolution.

Also it remains at an acceptable level ($\leq$15%) in the presence of very steep profiles. However, the oscillating error is a steep function of Δ making good Abel inversion impossible for values of Δ beyond 2 cm for particularly steep profiles. The oscillating error is as large as the systematic error of Gorenflo-A for Δ = 3.5 cm. The reasons for this large increase of the oscillating error with decreasing spatial resolution is discussed in the next section.

10. The Error Transmission

The most striking feature of figures 14 and 23 is the rapid increase of the oscillating error with decreasing spatial resolution (increasing Δ). Provided this error is not too large it may be reduced with a smoothing routine, sacrificing of course the fine structure.

The reason for the rapid increase of this error with Δ can be found in the increase of the Abel inversion matrix elements. Since the oscillating error for the hollow profiles is largest in the plasma centre, we only consider here the matrix elements A (I, J) for r = o or I = 1 as a function of the spatial resolution (Δ in cm), as shown in the figures 24 to 29. With increasing Δ it can be seen that, besides the increase of the matrix elements, there is also a broadening over r (or J). The large oscillations in the value of the matrix elements versus J for $\Delta \geq$ 3.5 cm are not fully understood. They could be due to too few steps for the integration over the solid angle. However, for $\Delta <$ 3 cm the integrations have been checked by reducing the number of steps by half, yielding essentially the same Abel inversion matrices.

It should be noted, that for smooth test functions (bell-shaped with r_2 = 6 cm and α = 4) a very good Abel inversion is obtained even for Δ = 4 cm, the error being less than one percent over most of the plasma cross-section. So, although the large oscillations of the matrix elements may be real (i.e. they are not due to some numerical problem), they will not be of further interest since in practice the error transmitted by the Abel inversion matrix with a resolution of 3 cm will be much larger. This can be shown with the aid of Fig.23: since the computing of the flux is in single precision and has a precision of about 10^{-5}, a test function with a depression of the order of 10^{-3} and matrix elements in the order of unity, would yield an error of 10^{-2}, as indeed can been seen in the figure. It can

readily be verified in this way that a large oscillating error corresponds to large matrix elements in the relevant Abel inversion matrix. Now consider an optimistic measured radial flux profile of 5×10^{-3} accuracy. The error (not necessarily oscillating), after Abel inversion for $\Delta = 3$ cm and an expected depression of the hollow profile of 10^{-3}, is then a factor of 200 for the values in the centre. Thus, a detector system with a bad spatial resolution is not particularly suitable for measuring the central value of hollow profiles.

For $\Delta = 3$ cm we have found that the error is multiplied by a factor of hundred. So in the case of bad spatial resolution the use of Gorenflo-A or equivalent methods will mask the real error on the Abel inverted profiles.

11. Conclusion

It has been found, that for hollow and for bell-shaped radial intensity profiles the newly presented, second order and spatially resolved Abel inversion routine leads to a marked improvement over present methods. This improvement is typically a factor of 25, although, for those profiles for which the classical Abel inversion method works satisfactorily, this improvement is not so important. The method presented here is particularly applicable to profiles with steep gradients and/or hollow centres.

Since spatial resolution of each detector is taken into account detectors with wider acceptance angles and therefore greater flux input can be used. Also fewer detectors are needed to achieve the same accuracy of previous methods.
Also a major advantage of this method over previous methods is that the transfer of errors in the flux data is handled correctly. Thus, the errors are not masked as is the case when using Gorenflo-A for a detector with a wide acceptance angle.

Acknowledgement

The author is grateful to Dr. J. How for carefully reading the manuscript.

Reference

[11] Gorenflo, R., IPP-Report IPP 6/19, Mai 1964

Figure Captions

Fig.1 General view of a two slit detection system showing the actual volume of the cylindrical plasma seen by the detector.

Fig.2 The detailed geometry of the detection system used in the computer program.

Fig.3 Elements of the Abel-integral matrix $\alpha(n,i)$ used in Gorenflo-A.

Fig.4 The allocation of volume elements to the Abel integral matrix elements as in figure 3.

Fig.5 Radial profiles of the local intensity I and its flux Φ with $r_2 = 6$ cm and $\alpha = 4$ for an infinite spatial resolution. The plasma radius a is 11 cm.

Fig.6 The error ε as function of the radius due to Gorenflo-A for the functions shown in Fig.5.

Fig.7 The error ε as function of the radius due to the extended Abel inversion for the functions in Fig.5.

Fig.8 Radial profiles of the local intensity I and its flux Φ with $r_2 = 6$ cm and $\alpha = 16$ for an infinite spatial resolution.

Fig.9 The error ε as a function of the radius due to Gorenflo-A for the functions shown in Fig.8.

Fig.10 The error ε as a function of the radius due to the extended Abel inversion for the functions shown in Fig.8.

Fig.11 The flux Φ as function of the radius for detection systems with different spatial resolution. $\Delta = 0$ and 4 cm respectively and with $r_2 = 6$ cm and $\alpha = 16$.

Fig.12 The error ε as function of the radius due to Gorenflo-A for a steep radial intensity profile ($r_2 = 6$ cm, $\alpha = 16$) and a poor spatial resolution ($\Delta = 3$ cm).

Fig.13 The error ε as function of the radius due to the extended Abel inversion for the function used in Fig.12. The systematic error (dashed line) is sketched into the figure.

Fig.14 The maximal error due to Gorenflo-A (trace a), the maximal systematic error due to the extended Abel inversion for $r \sim 10$ cm (trace b) and its oscillating error (trace c) as a function of the spatial resolution Δ for a steep radial profile ($r_2 = 6$ cm and $\alpha = 16$).

Fig.15 The maximal error due to Gorenflo-A (trace a), the maximal systematic error due to the extended Abel inversion for $r \sim 10$ cm (trace b) and its oscillating error (trace c) as a function of the spatial resolution Δ for smooth radial profiles ($r_2 = 6$ cm and $\alpha = 4$).

Fig.16 The radial hollow intensity profile I with $I_o = 10^{-4}$, $r_2 = 6$ cm, $\alpha = 16$ and $\delta = 0.5$ cm.

Fig.17 The same radial intensity profile as in Fig.16 given on a linear scale and its radial flux profile (c). Curve (a) and (b) are the radial flux profiles for radial intensity distributions with $I_o = 10^{-1}$ and 10^{-2} respectively. The curve for $I_o = 10^{-3}$ coincides with that for $I_o = 10^{-4}$. All curves are for ideal spatial resolution.

Fig.18 The dependence of the systematic error for Gorenflo-A on the central depression I_o at different radial positions for ideal spatial resolution

curve a: $0 < r < 2$ cm

curve b: $2 < r < 5$ cm

curve c: $7 < r < 10$ cm (peak position)

Fig.19 The saturation of the central intensity after Gorenflo-A Abel inversion with the decreasing real central intensity dependent on the number of points used in the inversion.

Fig.20 The central intensity after Gorenflo-A Abel inversion for two real central intensities: $I(o) = 10^{-3}$ and 10^{-4} respectively as a function of the number of points used in the inversion.

Fig.21 The maximum systematic error ε due to the extended Abel inversion as a function of the central value of the intensity I (o) at different radial positions for ideal spatial resolution.

curve a: $0 < r < 2,5$ cm

curve b: $2,5 < r < 5$ cm

curve c: $5 < r < 10$ cm (peak position)

(Compare Fig.18.)

Fig.22 The systematic error ε by Gorenflo-A for various radial positions as a function of the spatial resolution

curve a: $r \sim 0$ cm

curve b: $r \sim 3,5$ cm

curve c: $r \sim 8$ cm

Fig.23 The oscillating error (curve a) and the systematic error (curve b and c) by the extended Abel inversion as a function of the spatial resolution.

curve b: $2 < r < 5$ cm

curve c: $5 < r < 10$ cm

Fig.24 to 29 The Abel inversion matrix elements A (1, J) as a function of J (I = 1 for r = 0 cm) for several spatial resolutions Δ as marked in each figure. Elements marked ● are positive, those marked o are negative. Note the strong increase of the absolute value of the matrix elements when going from Δ = 1 to 3 cm and then the strong oscillations of the absolute values for $\Delta > 3$ cm.

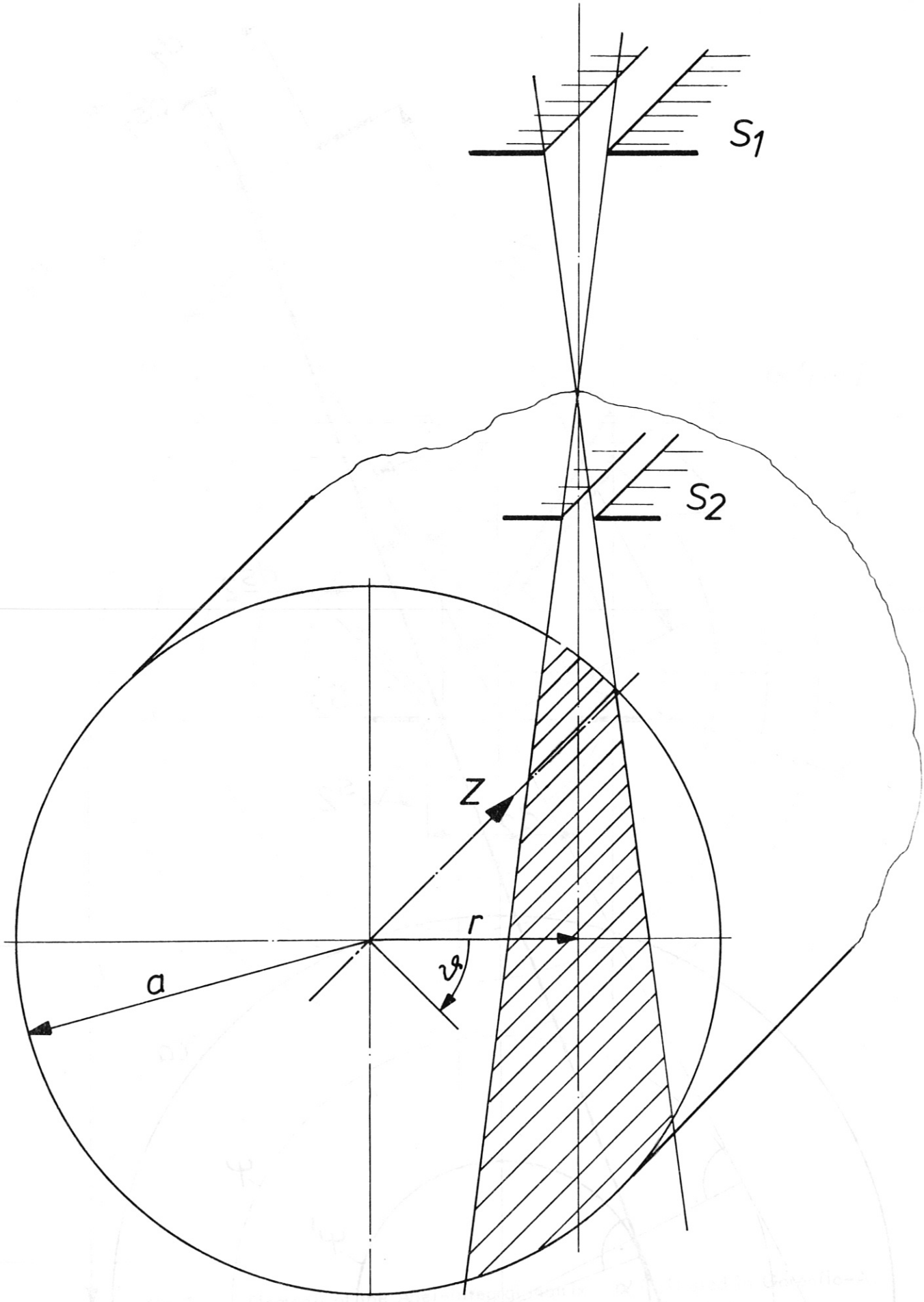

Fig. 1 General view of a two slit detection system showing the actual volume of the cylindrical plasma seen by the detector.

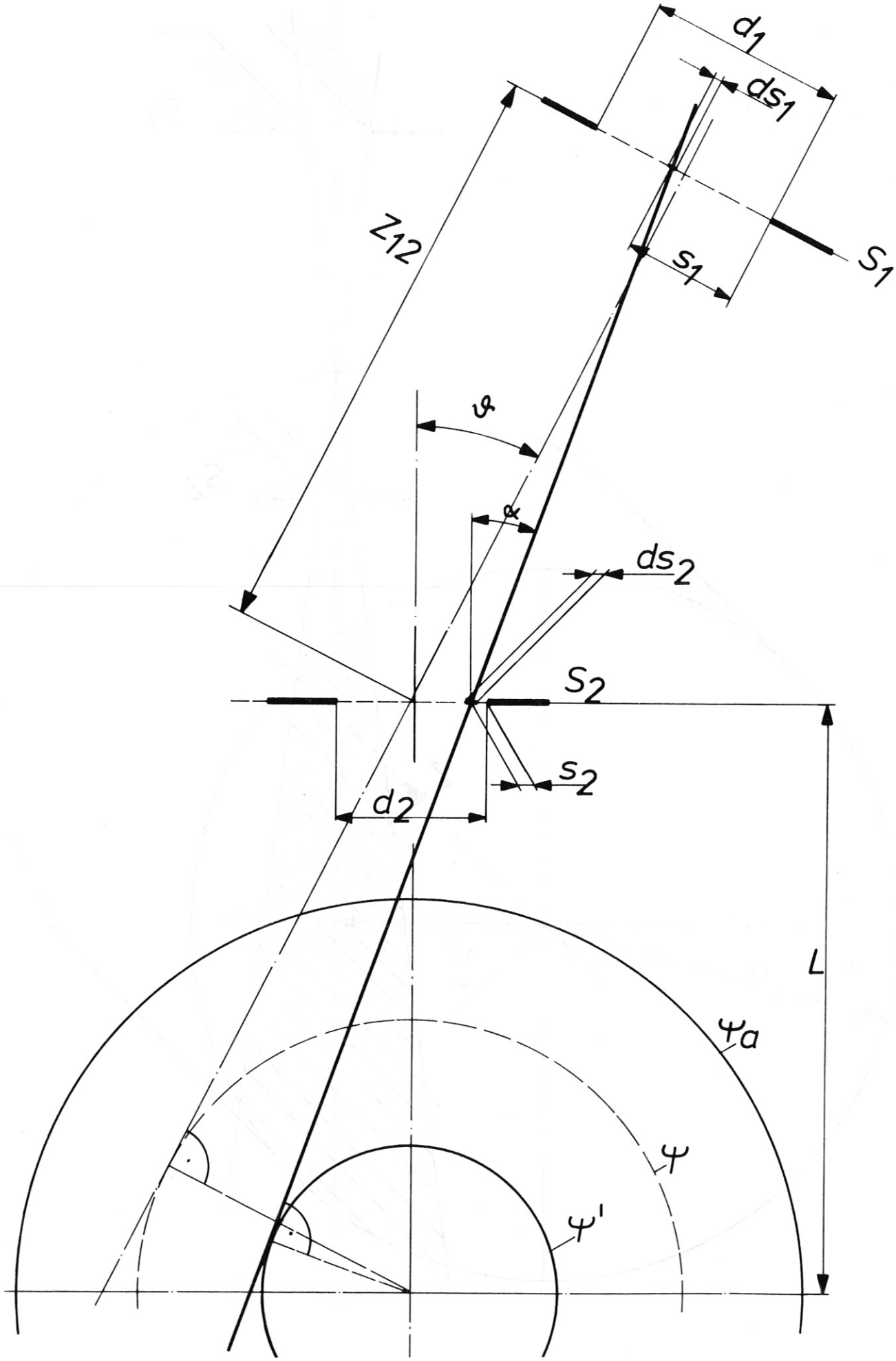

Fig.2 The detailed geometry of the detection system used in the computer program.

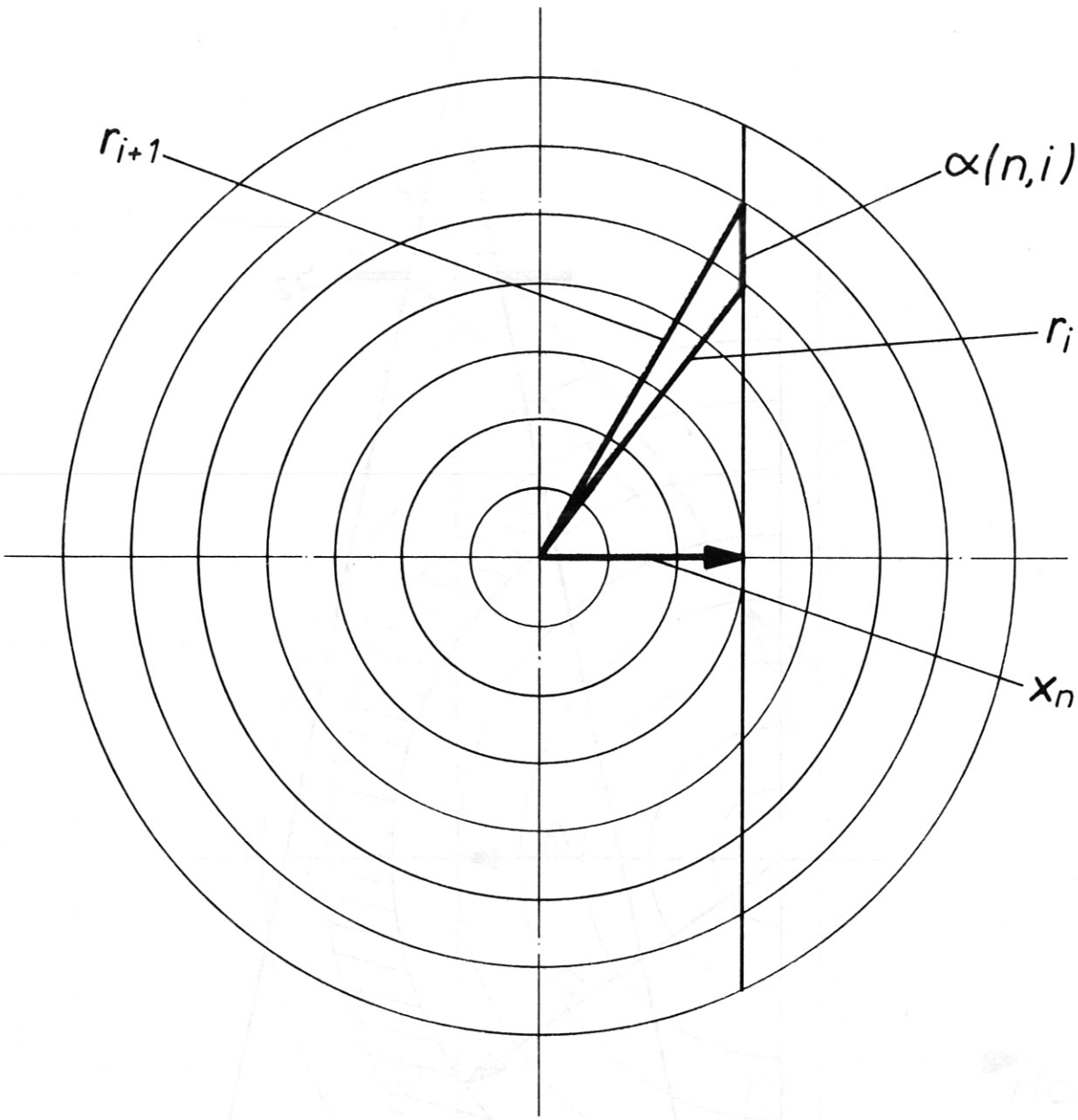

Fig.3 Elements of the Abel-integral matrix $\alpha(n,i)$ used in Gorenflo-A.

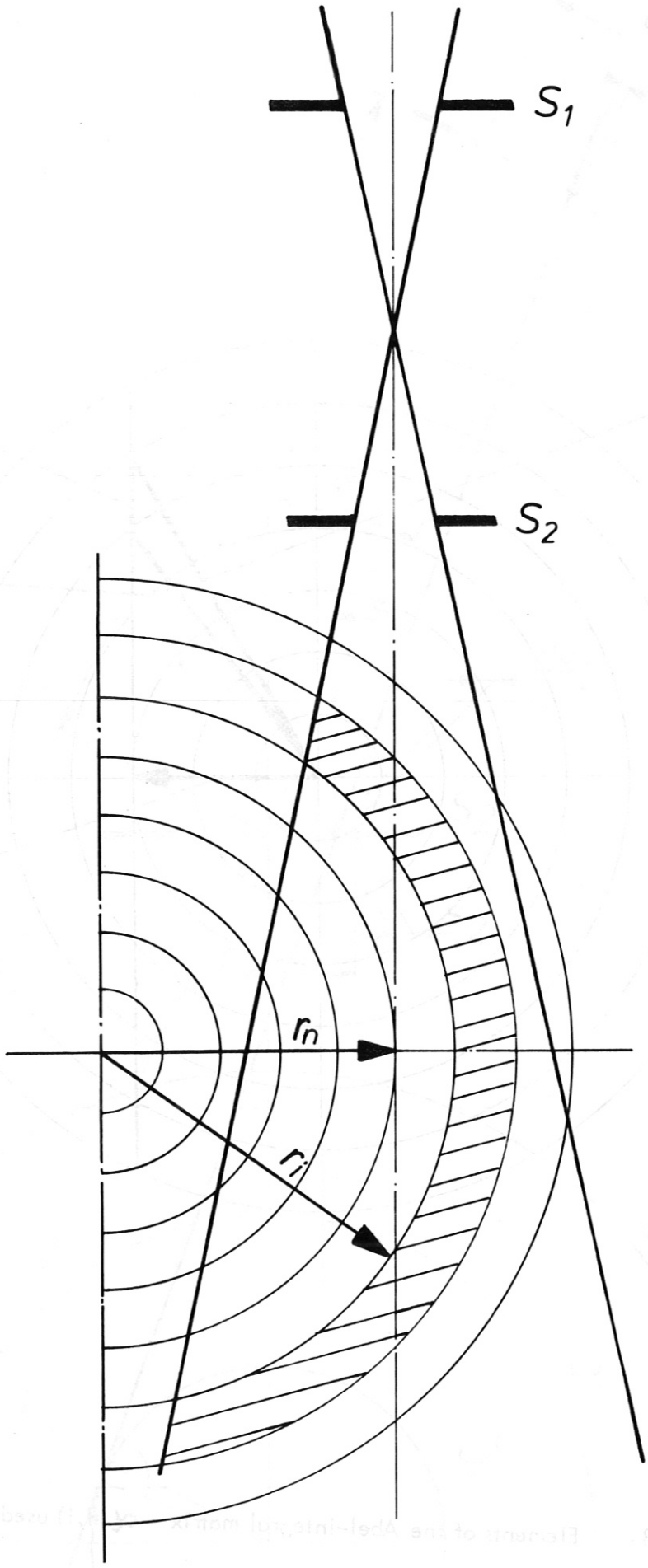

Fig.4 The allocation of volume elements to the Abel integral matrix elements as in figure 3.

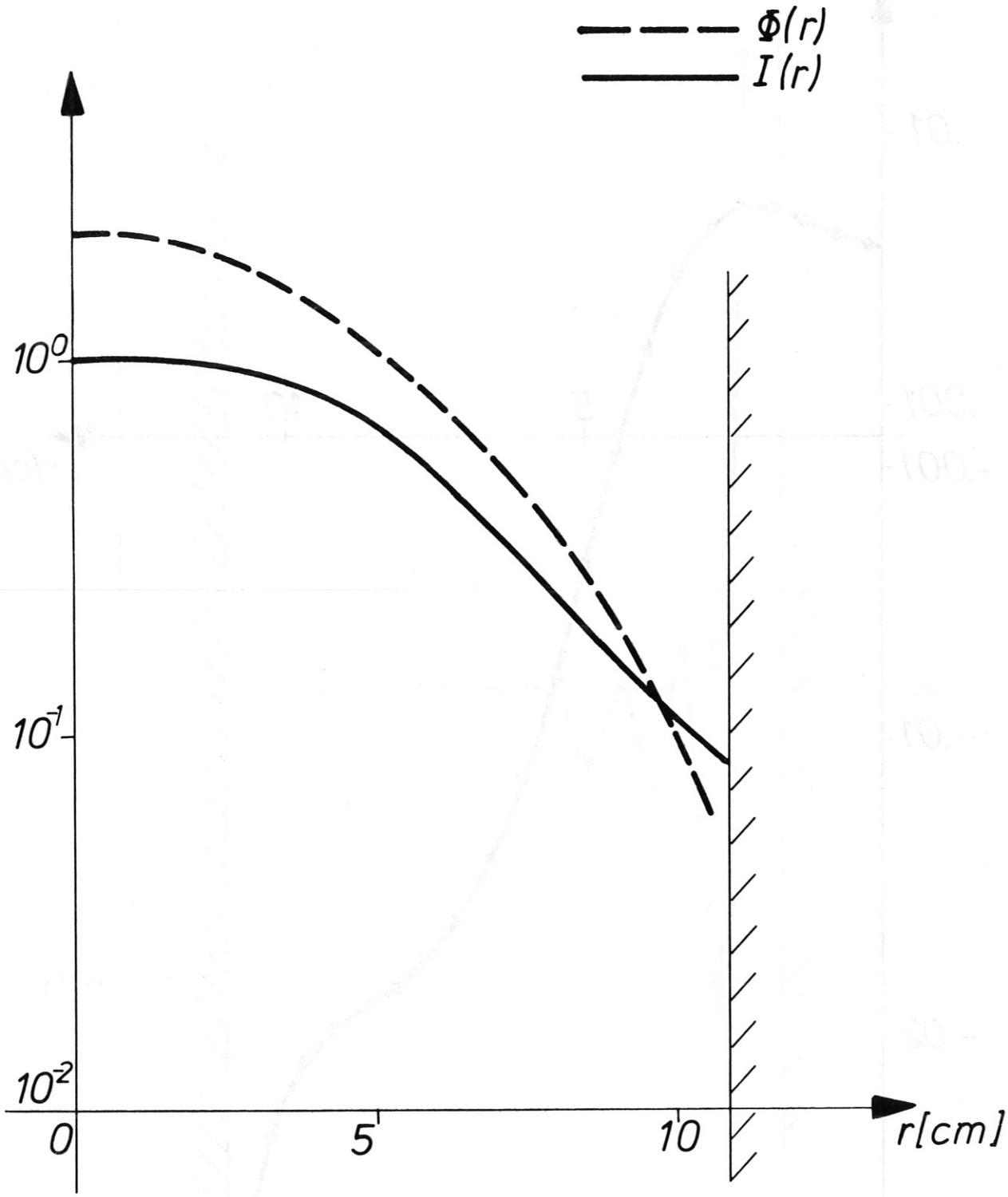

Fig.5 Radial profiles of the local intensity and its flux Φ with r_2 = 6 cm and α = 4 for an infinite spatial resolution. The plasma radius a is 11 cm.

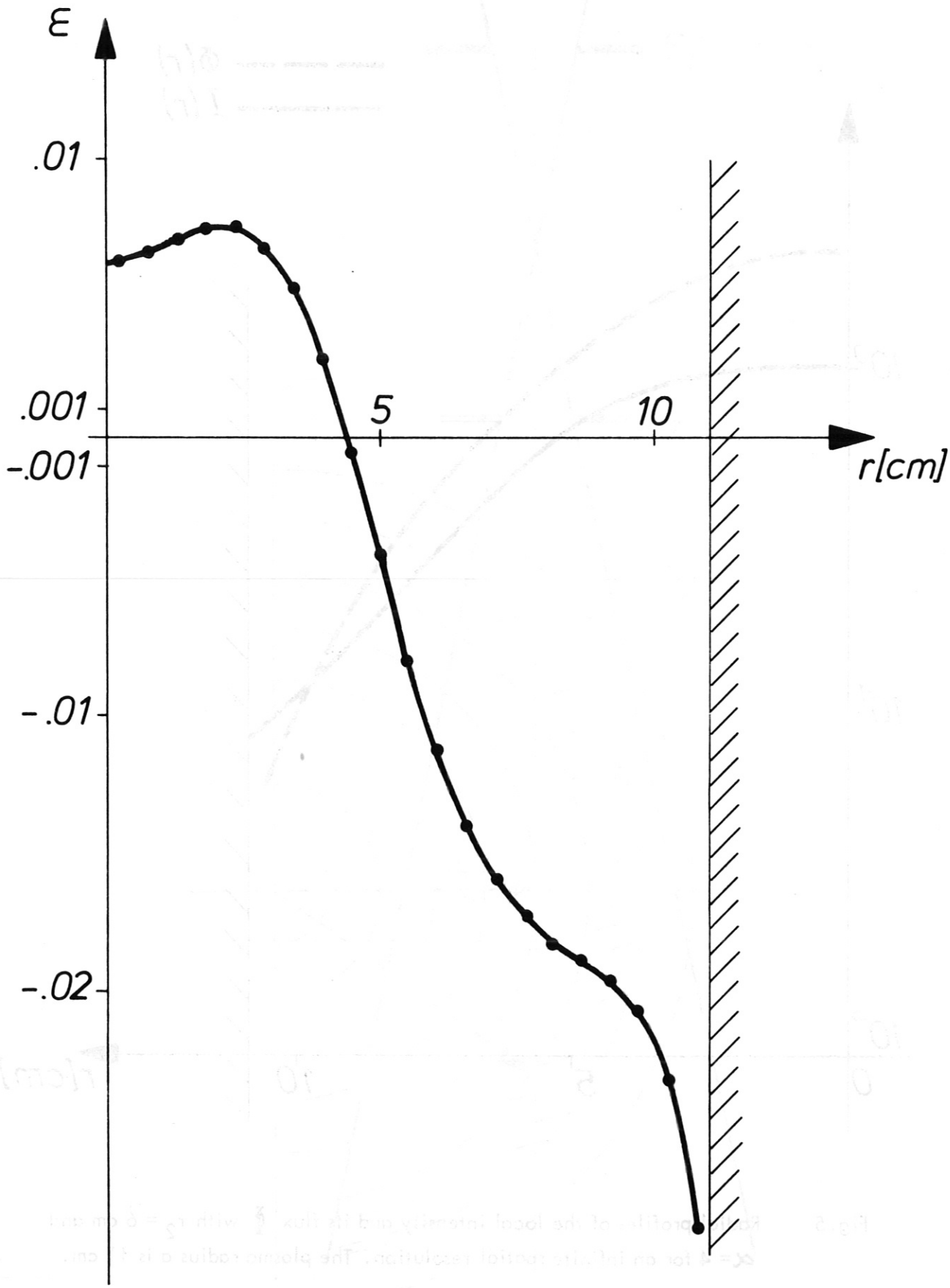

Fig.6 The error ε as function of the radius due to Gorenflo-A for the functions shown in Fig.5.

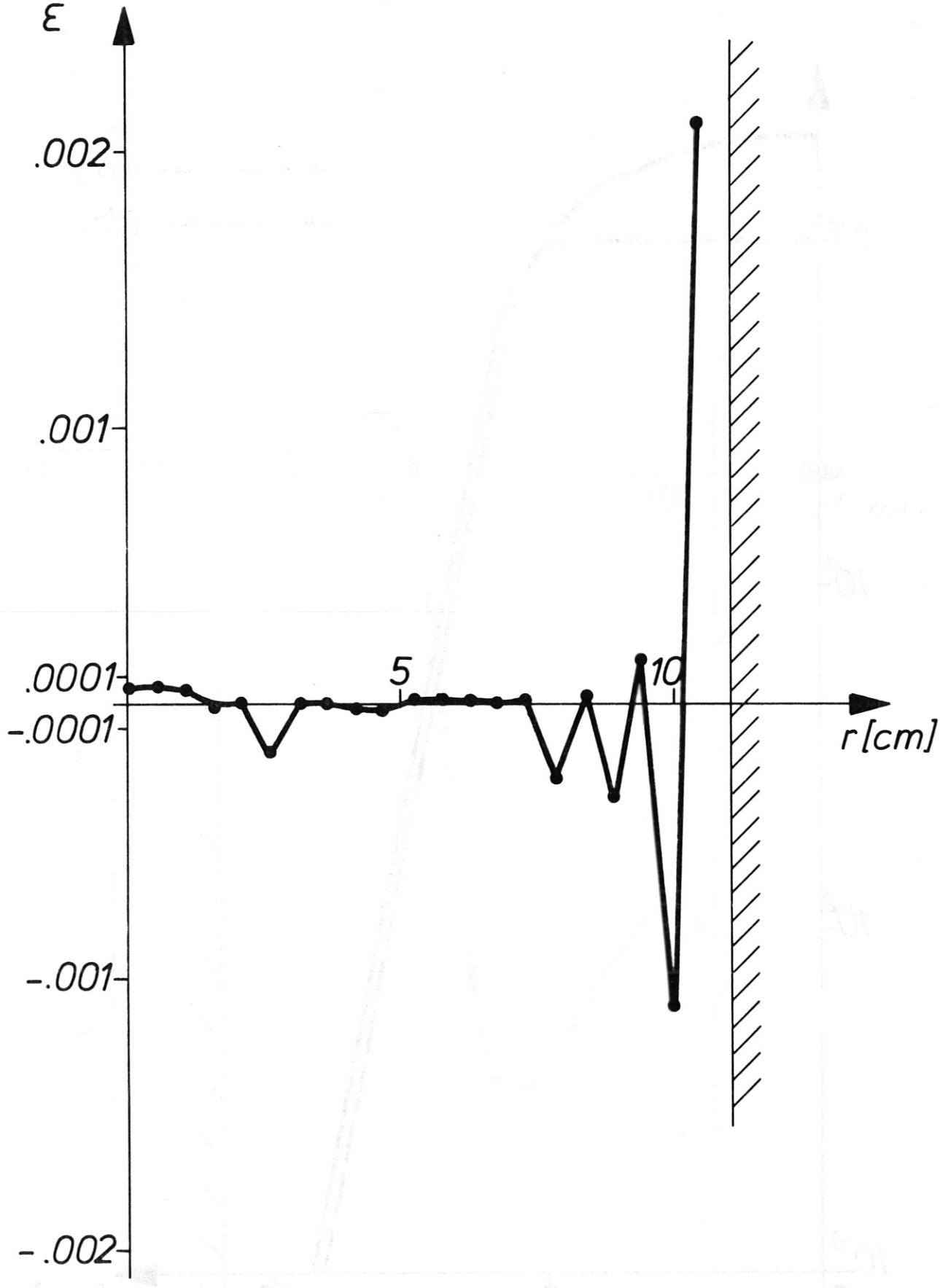

Fig.7 The error ε as function of the radius due to the extended Abel inversion for the functions in Fig.5.

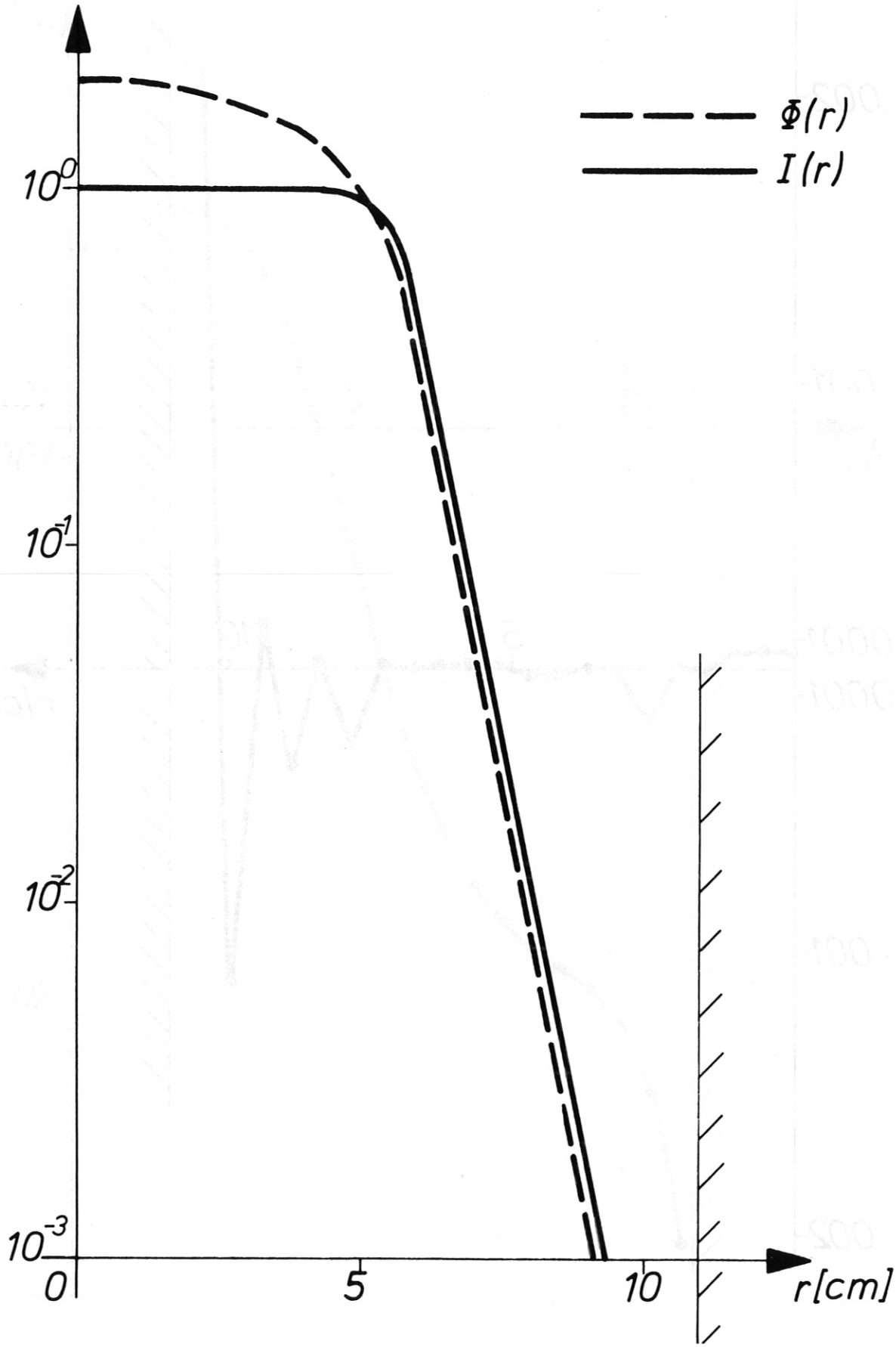

Fig.8 Radial profiles of the local intensity I and its flux Φ with r_2 = 6 cm and α = 16 for an infinite spatial resolution.

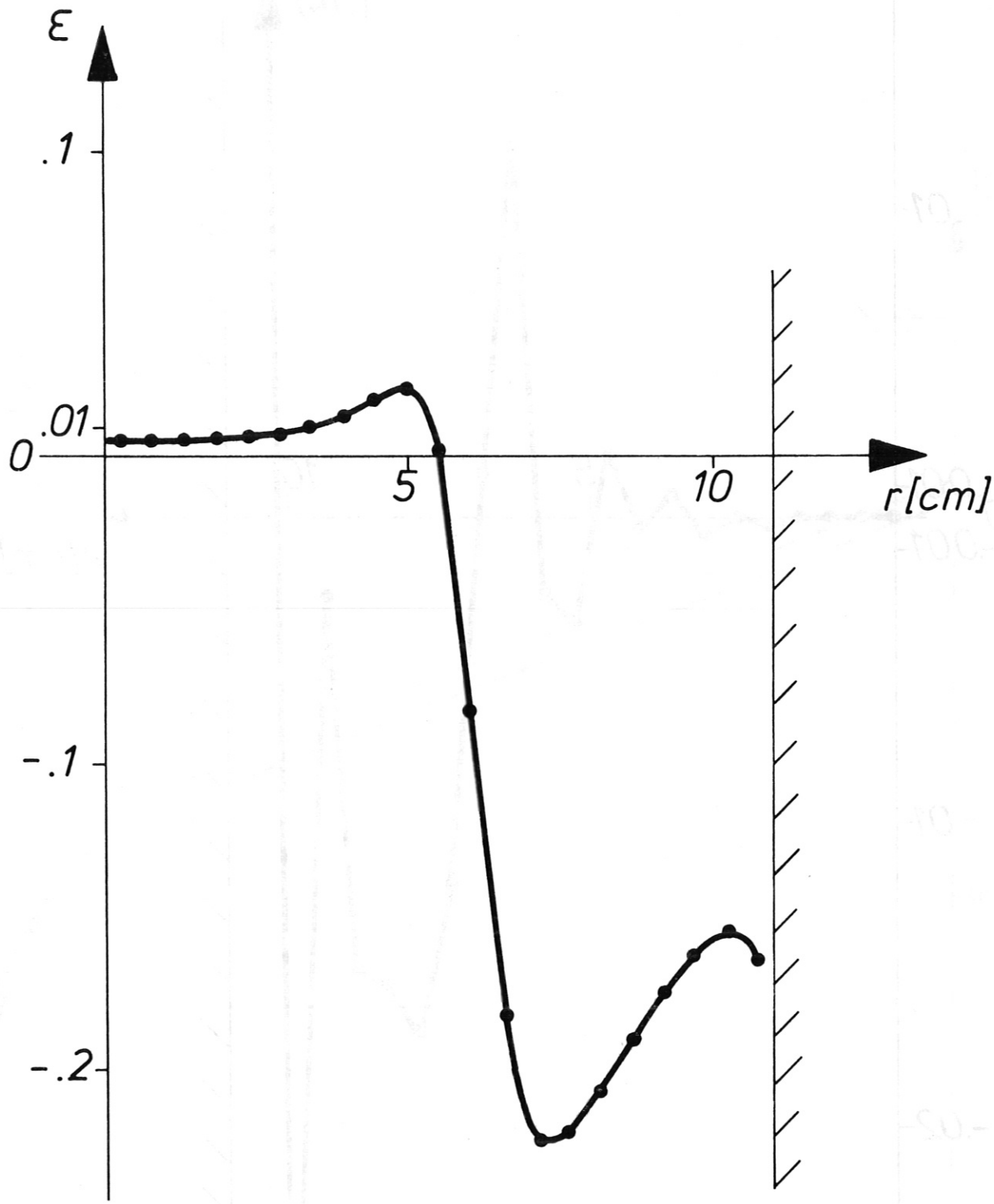

Fig.9 The error ε as a function of the radius due to Gorenflo-A for the functions shown in Fig.8.

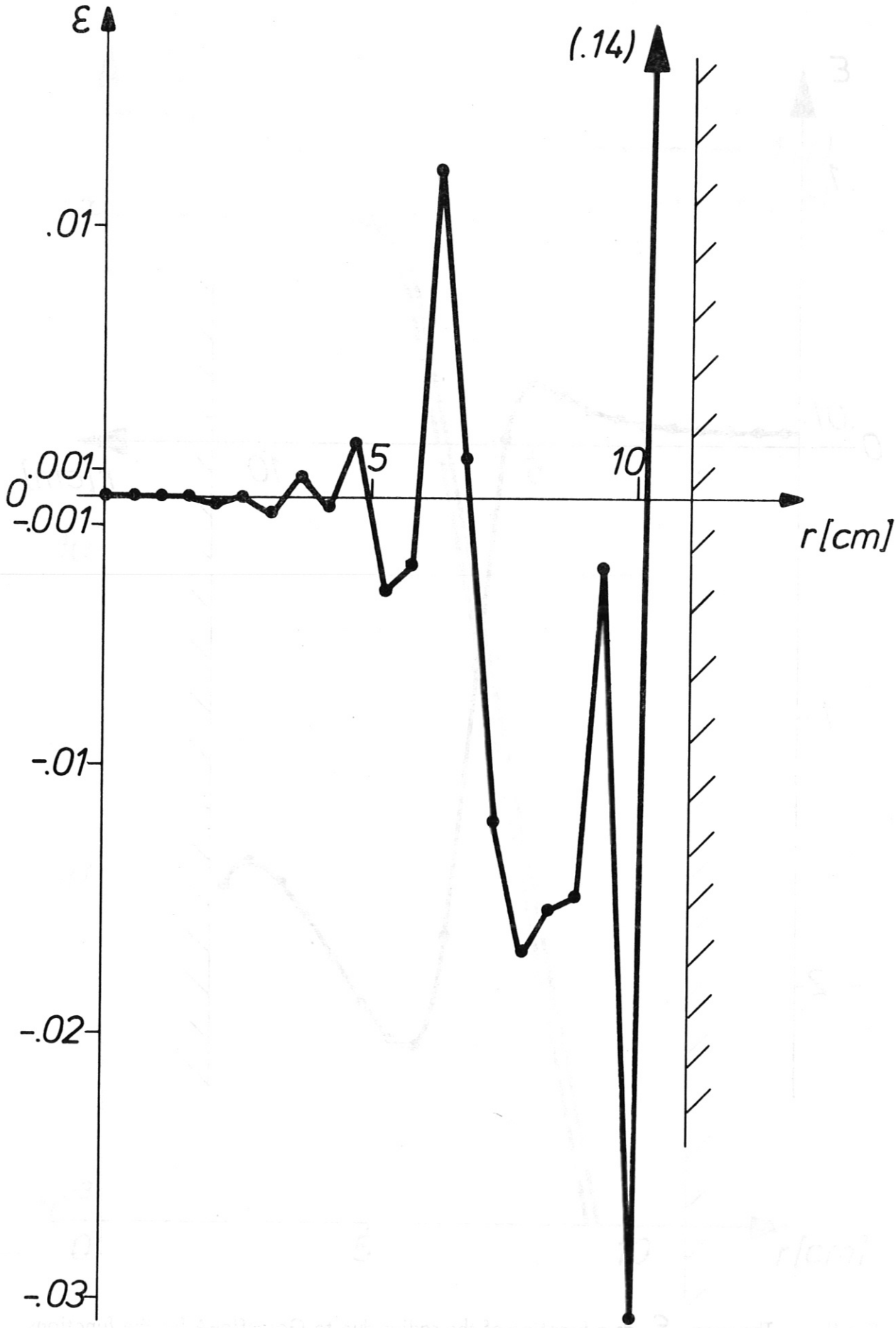

Fig.10 The error ε as a function of the radius due to the extended Abel inversion for the functions shown in Fig.8.

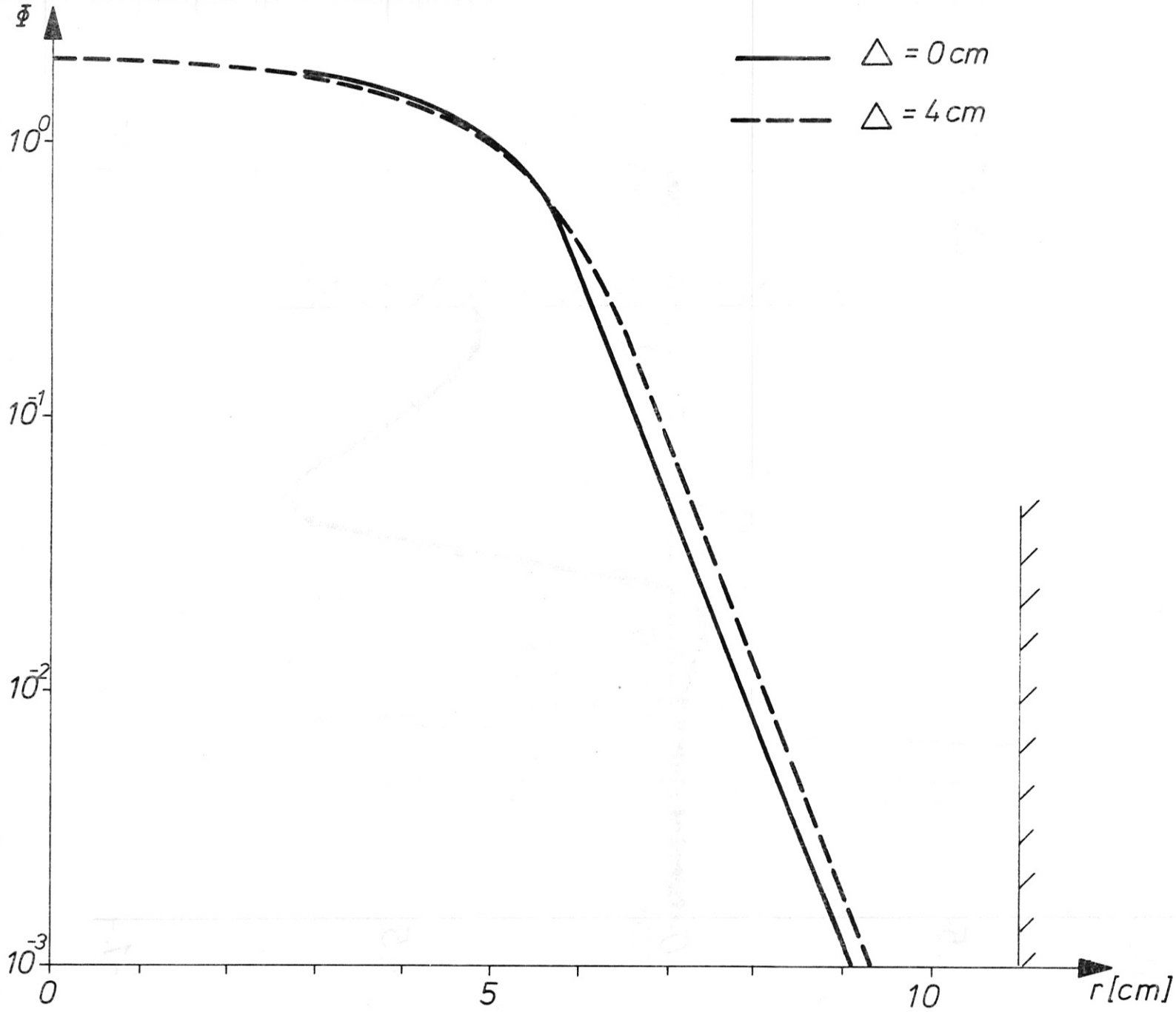

Fig.11 The flux Φ as function of the radius for detection systems with different spatial resolution, Δ = 0 and 4 cm respectively and with r_2 = 6 cm and α = 16.

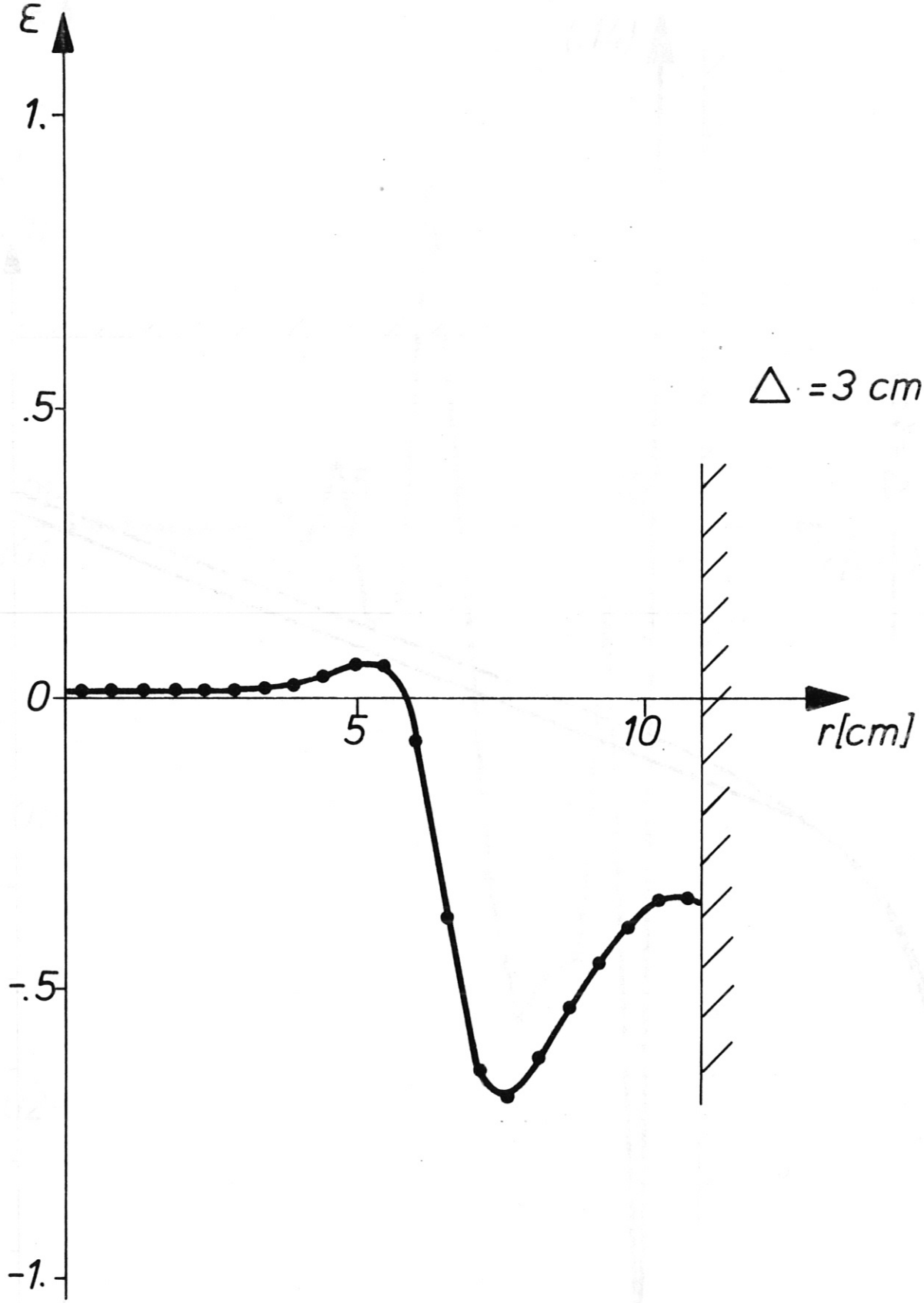

Fig. 12 The error ε as function of the radius due to Gorenflo-A for a steep radial intensity profile (r_2 = 6 cm, α = 16) and a poor spatial resolution (Δ = 3 cm).

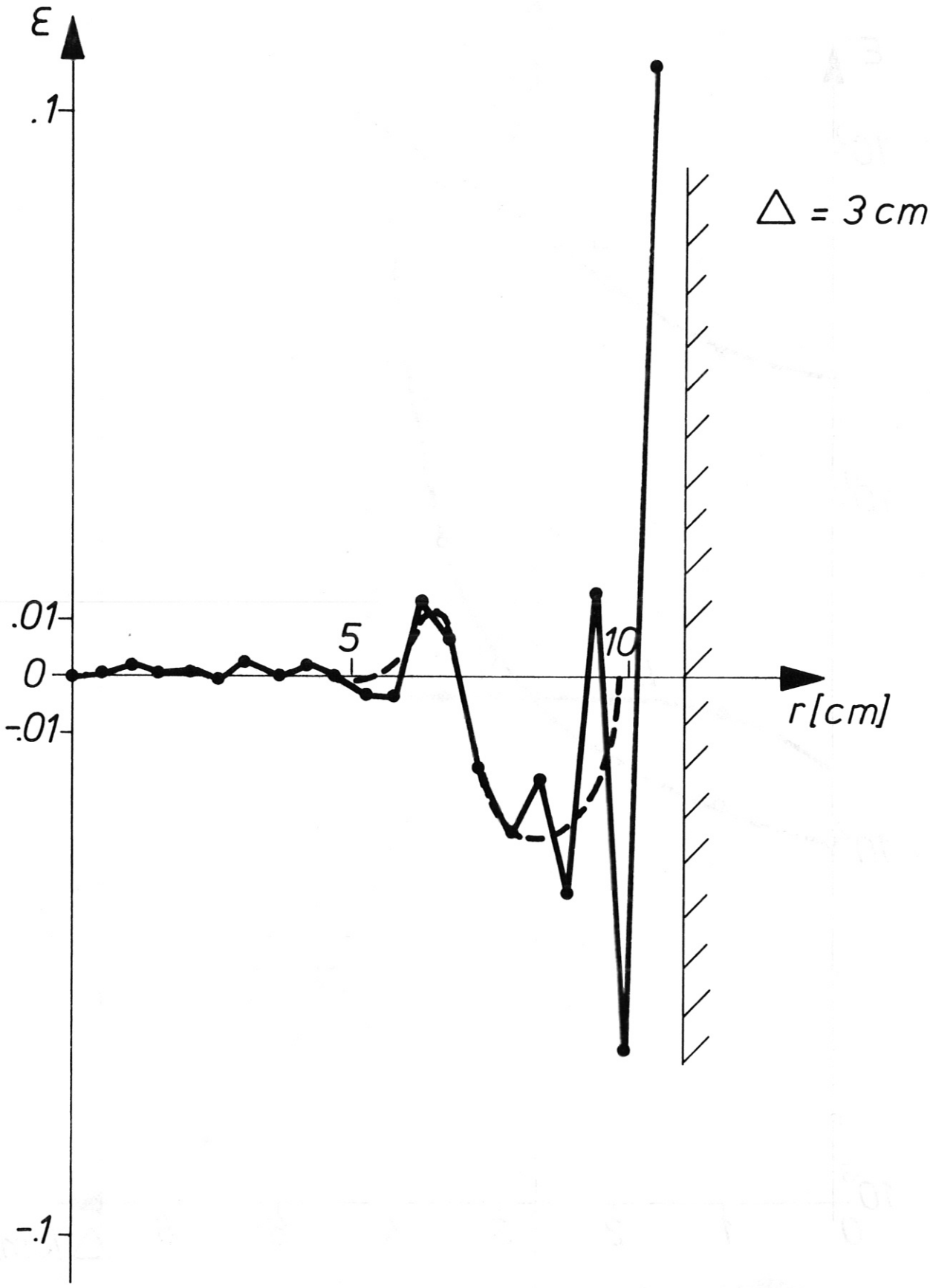

Fig.13 The error ε as function of the radius due to the extended Abel inversion for the function used in Fig.12. The systematic error (dashed line) is sketched into the figure.

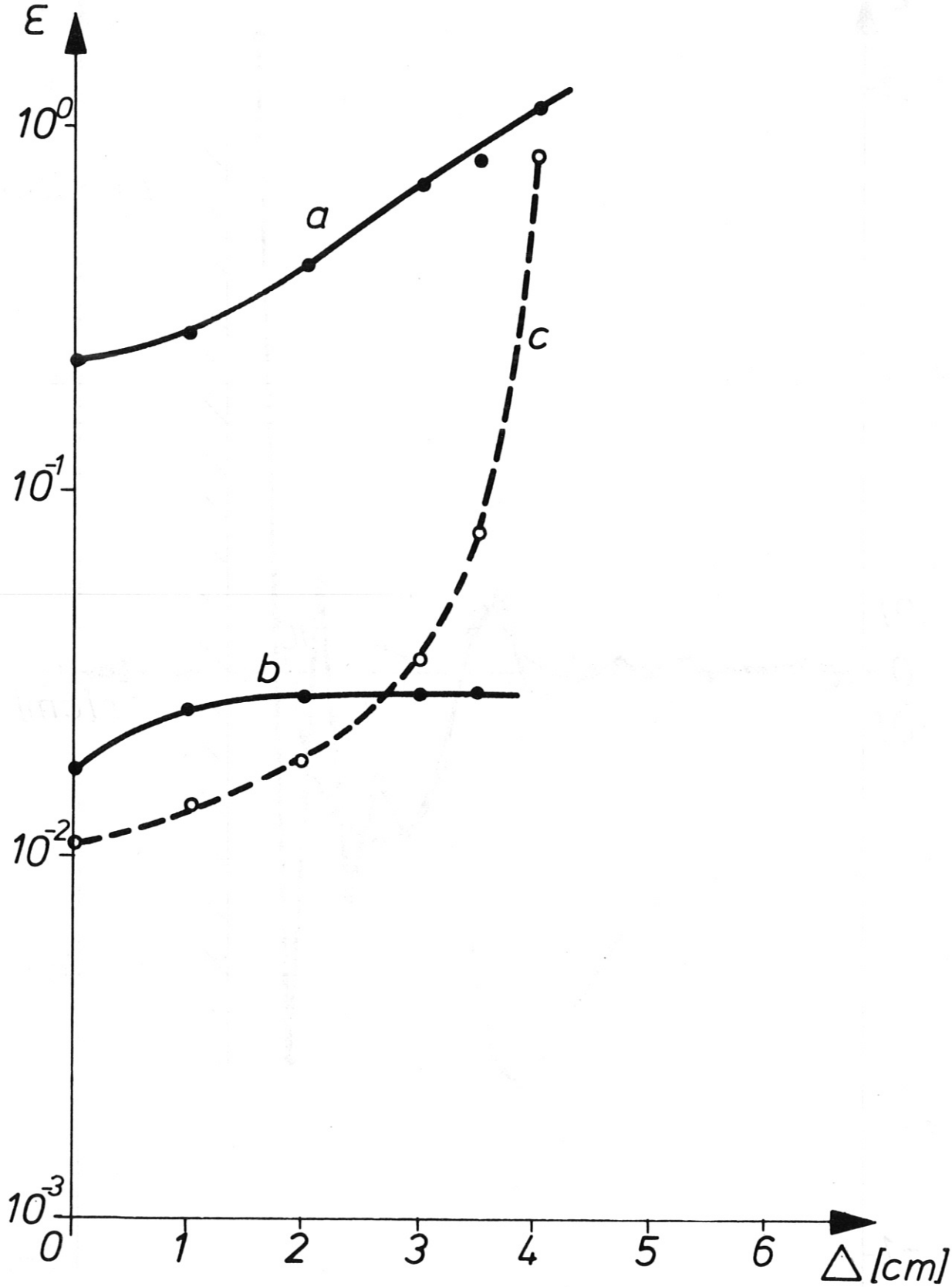

Fig. 14 The maximal error due to Gorenflo-A (trace a), the maximal systematic error due to the extended Abel inversion for r 10 cm (trace b) and its oscillating error (trace c) as a function of the spatial resolution Δ for a steep radial profile (r_2 = 6 cm and α = 16).

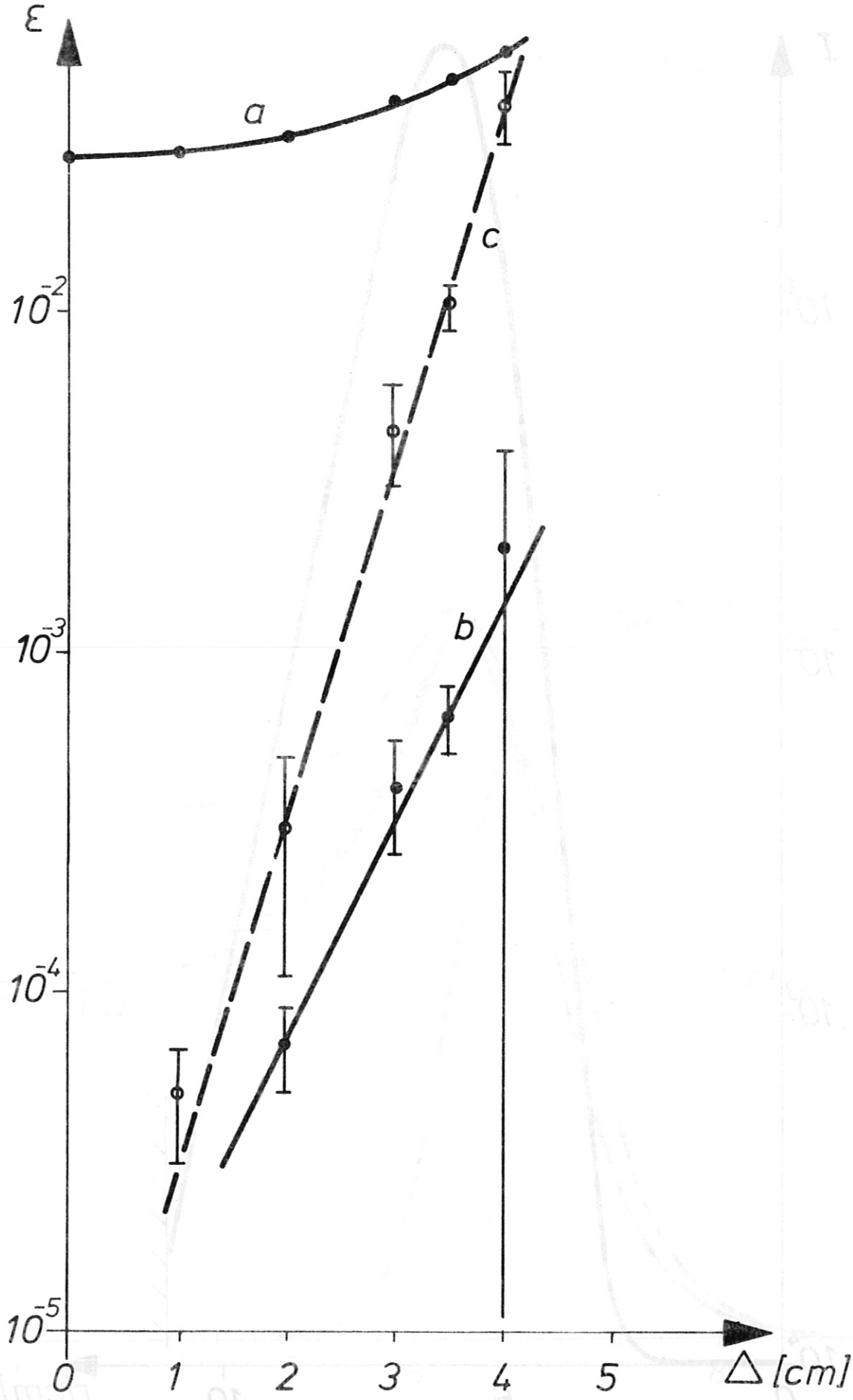

Fig.15 The maximal error due to Gorenflo-A (trace a), the maximal systematic error due to the extended Abel inversion for $r \sim 10$ cm (trace b) and its oscillating error (trace c) as a function of the spatial resolution Δ for smooth radial profiles ($r_2 = 6$ cm and $\alpha = 4$).

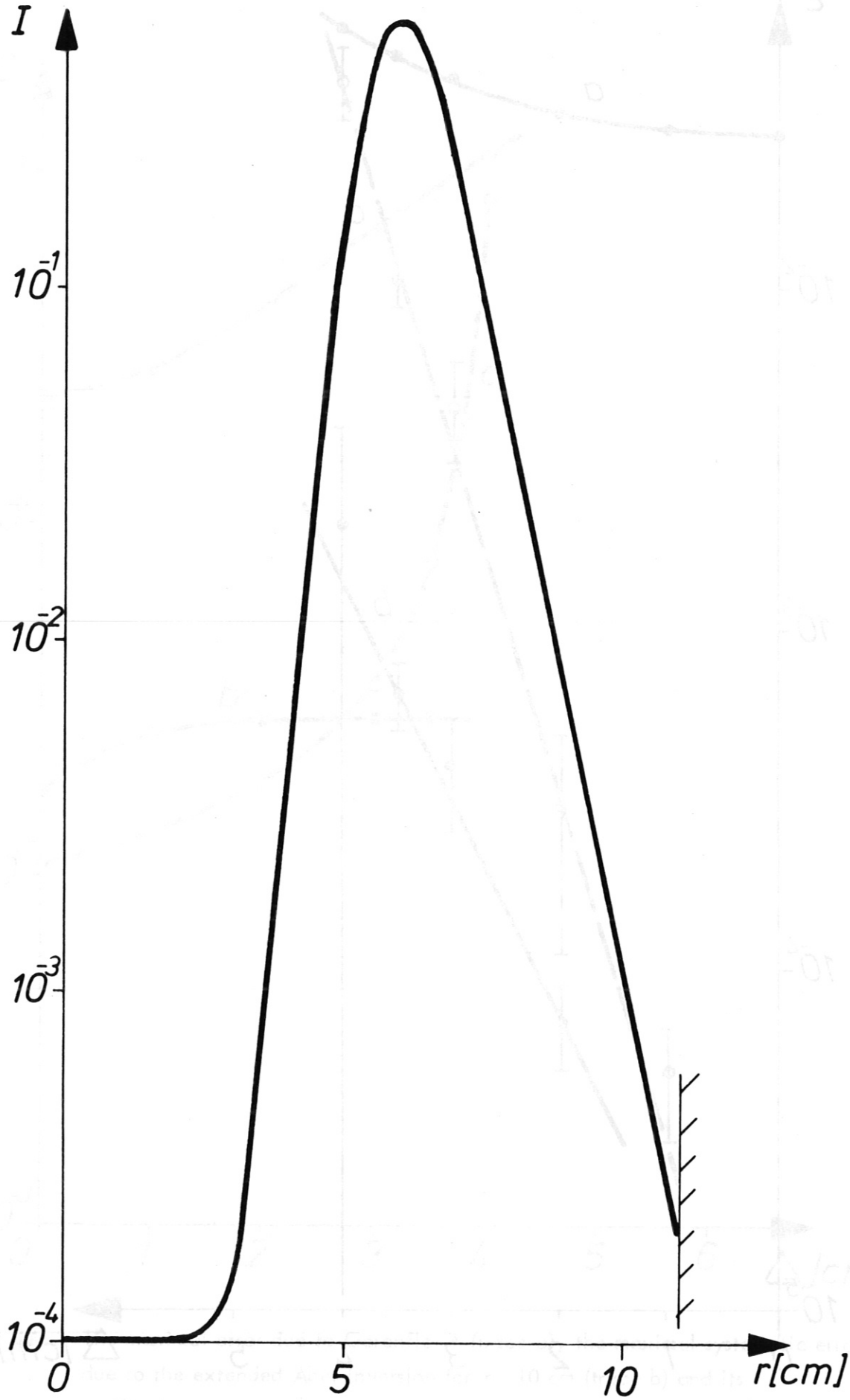

Fig. 16 The radial hollow intensity profile I with $I_o = 10^{-4}$, $r_2 = 6$ cm, $\alpha = 16$ and $\delta = 0.5$ cm.

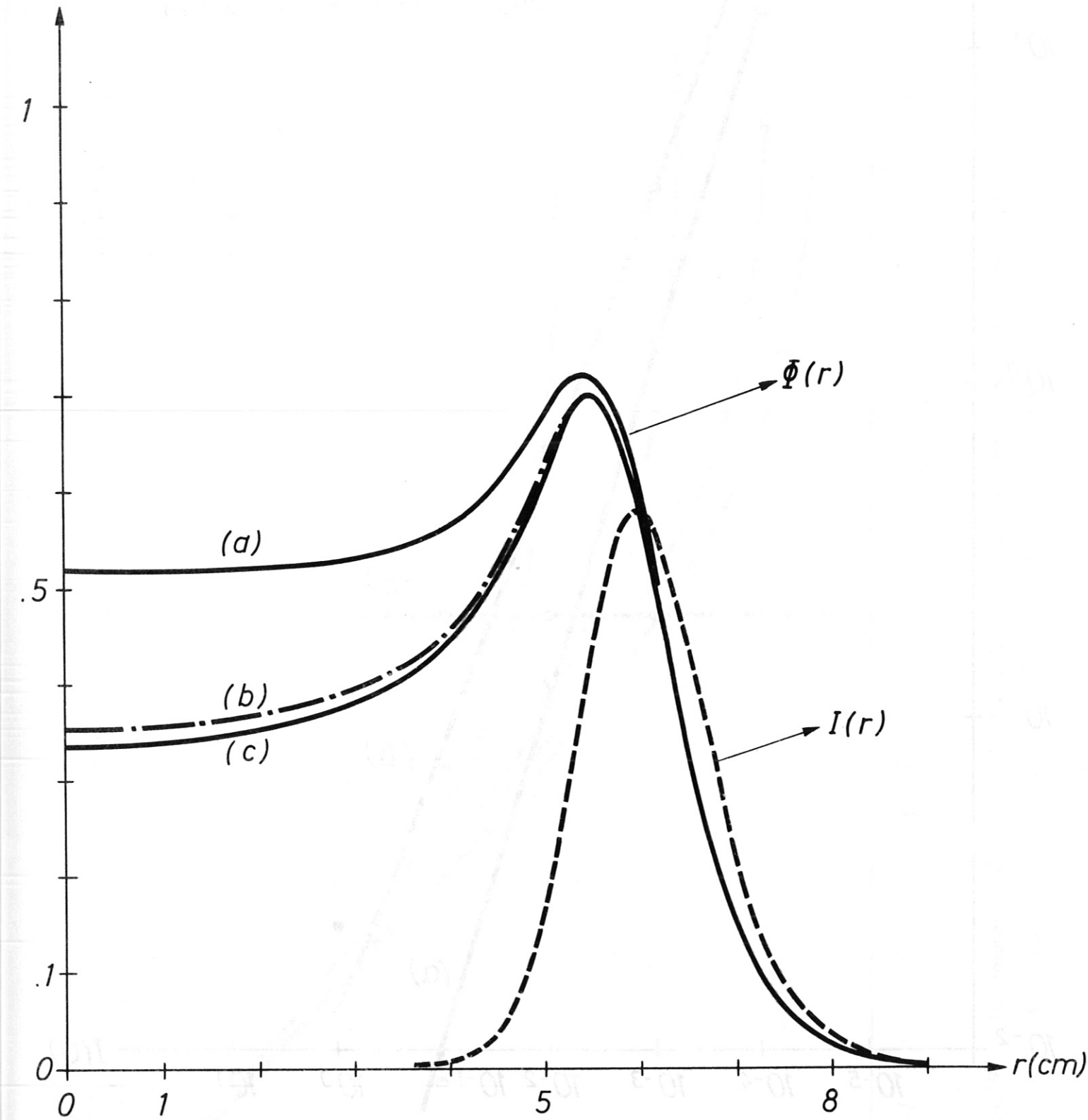

Fig. 17 The same radial intensity profile as in Fig. 16 given on a linear scale and its radial flux profile (c). Curve (a) and (b) are the radial flux profiles for radial intensity distributions with $I_o = 10^{-1}$ and 10^{-2} respectively. The curve for $I_o = 10^{-3}$ coincides with that for $I_o = 10^{-4}$. All curves are for ideal spatial resolution.

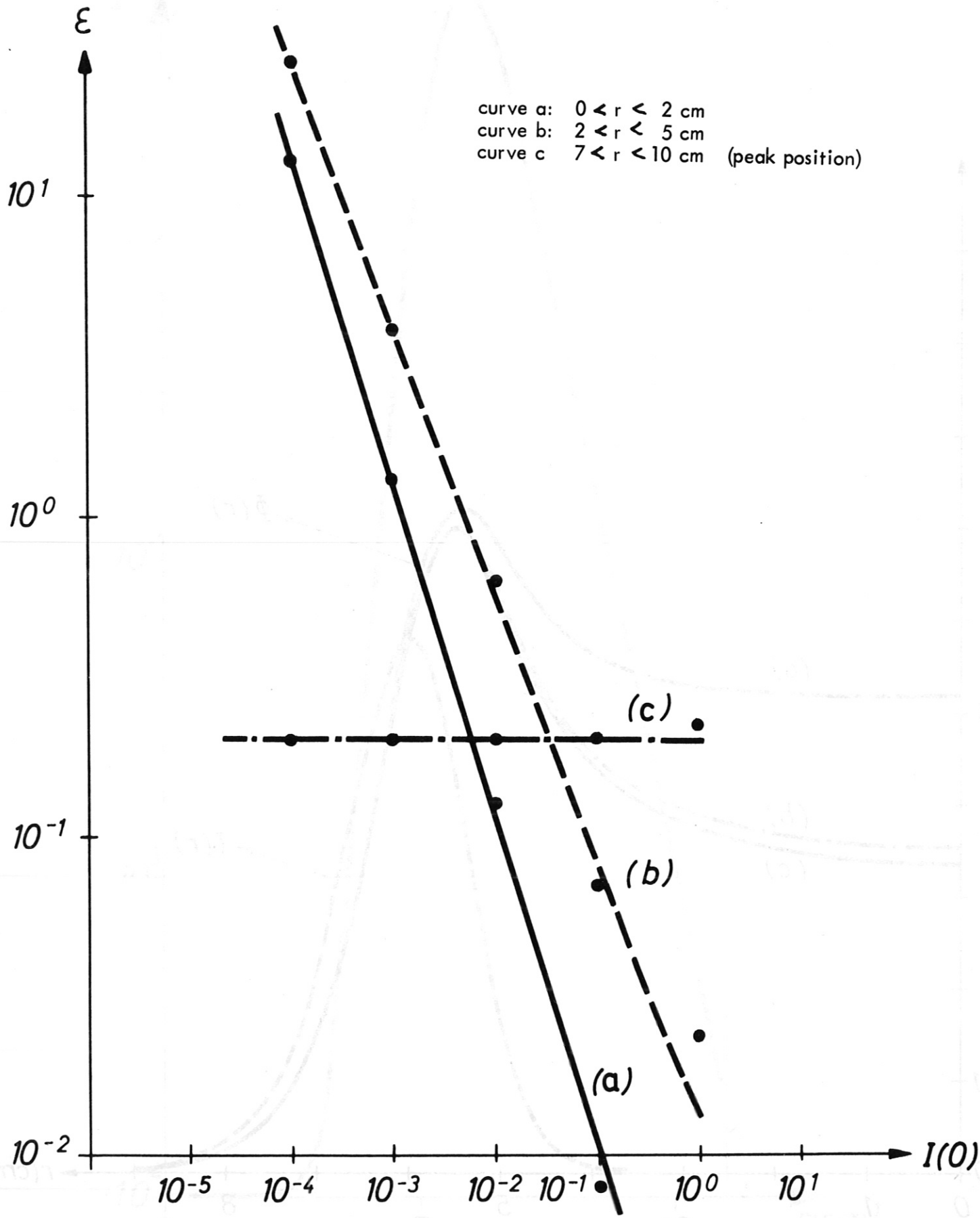

Fig.18 The dependence of the systematic error for Gorenflo-A on the central depression I_o at different radial positions for ideal spatial resolution

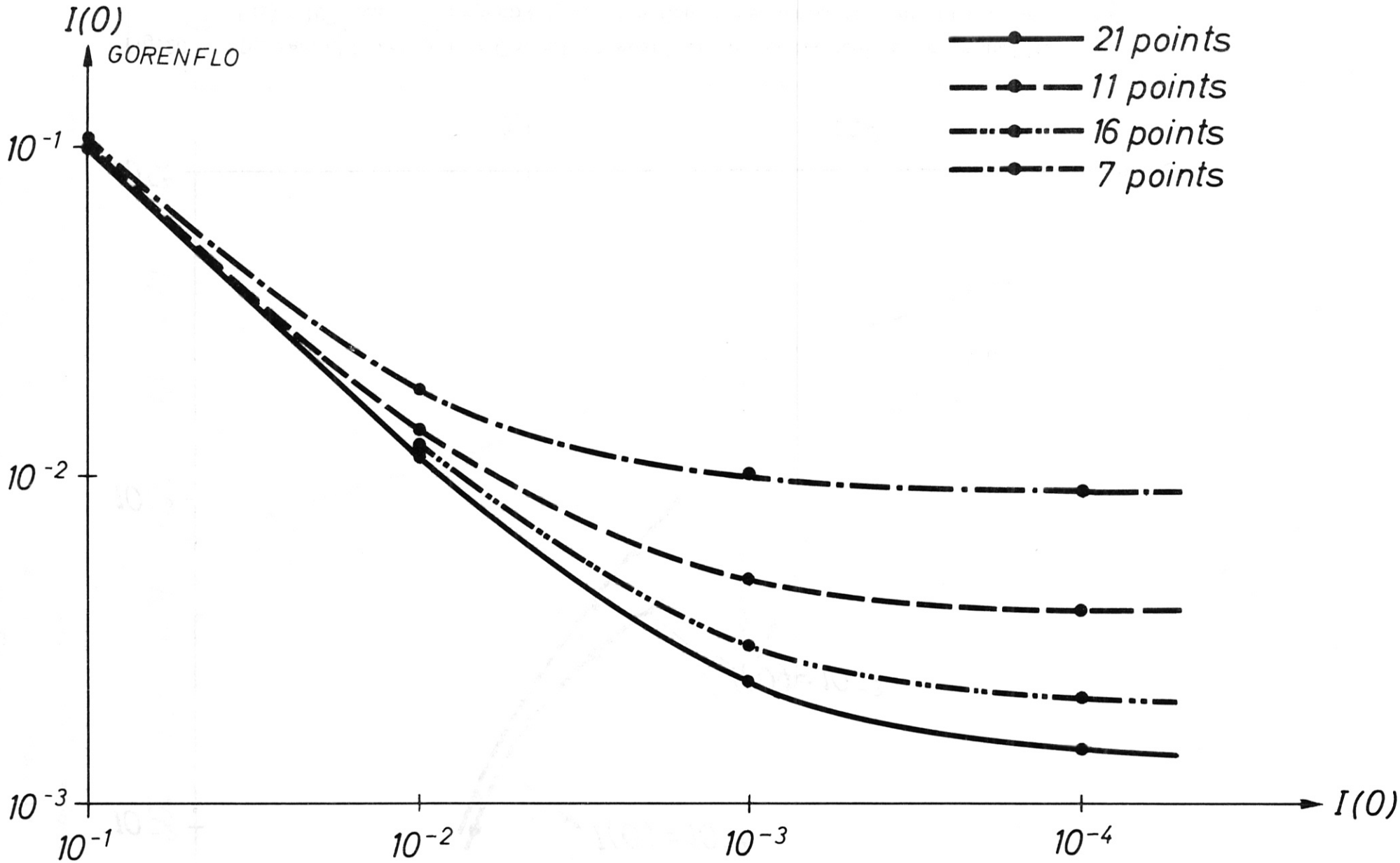

Fig. 19 The saturation of the central intensity after Gorenflo-A Abel inversion with the decreasing real central intensity dependent on the number of points used in the inversion.

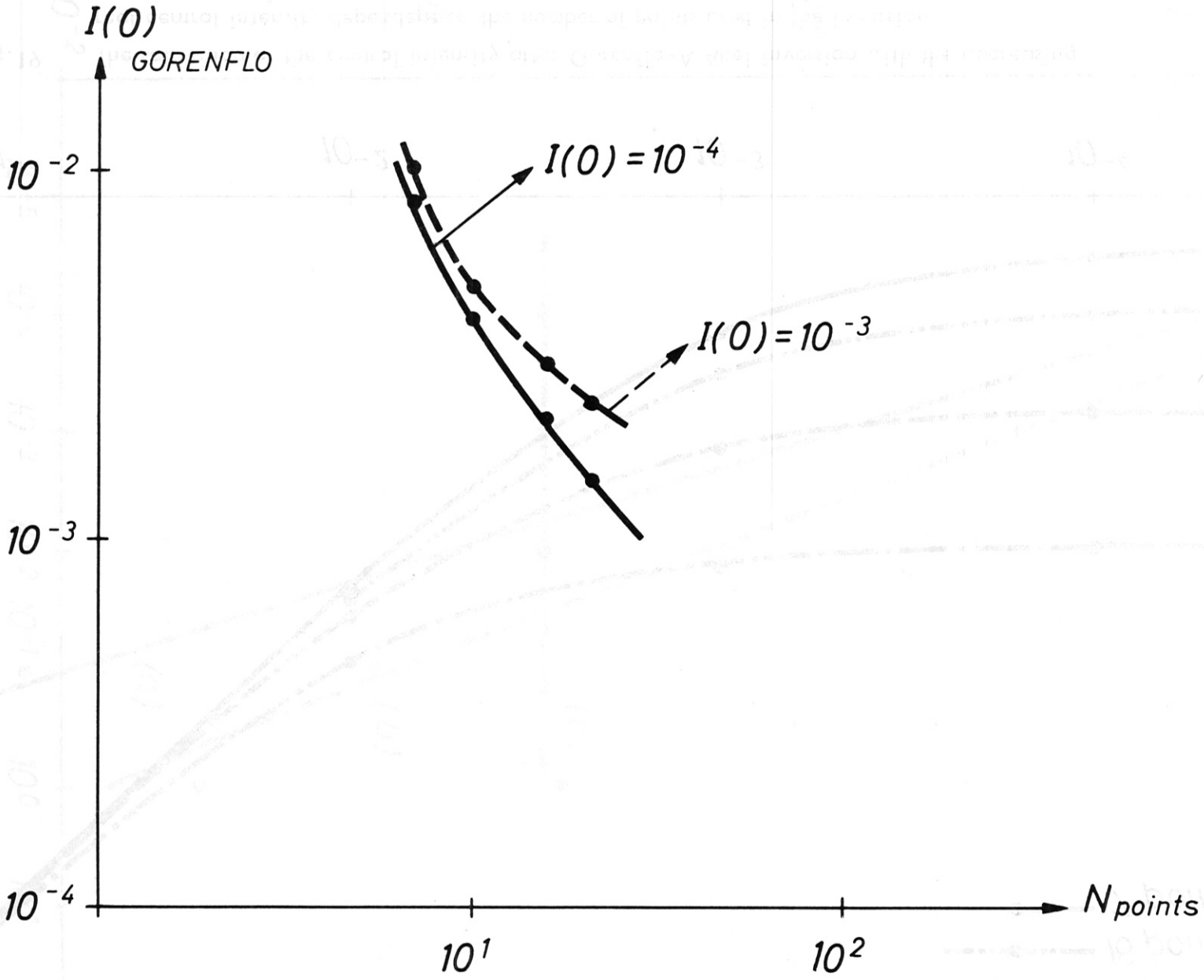

Fig.20 The central intensity after Gorenflo-A Abel inversion for two real central intensities: I (o) = 10^{-3} and 10^{-4} respectively as a function of the number of points used in the inversion.

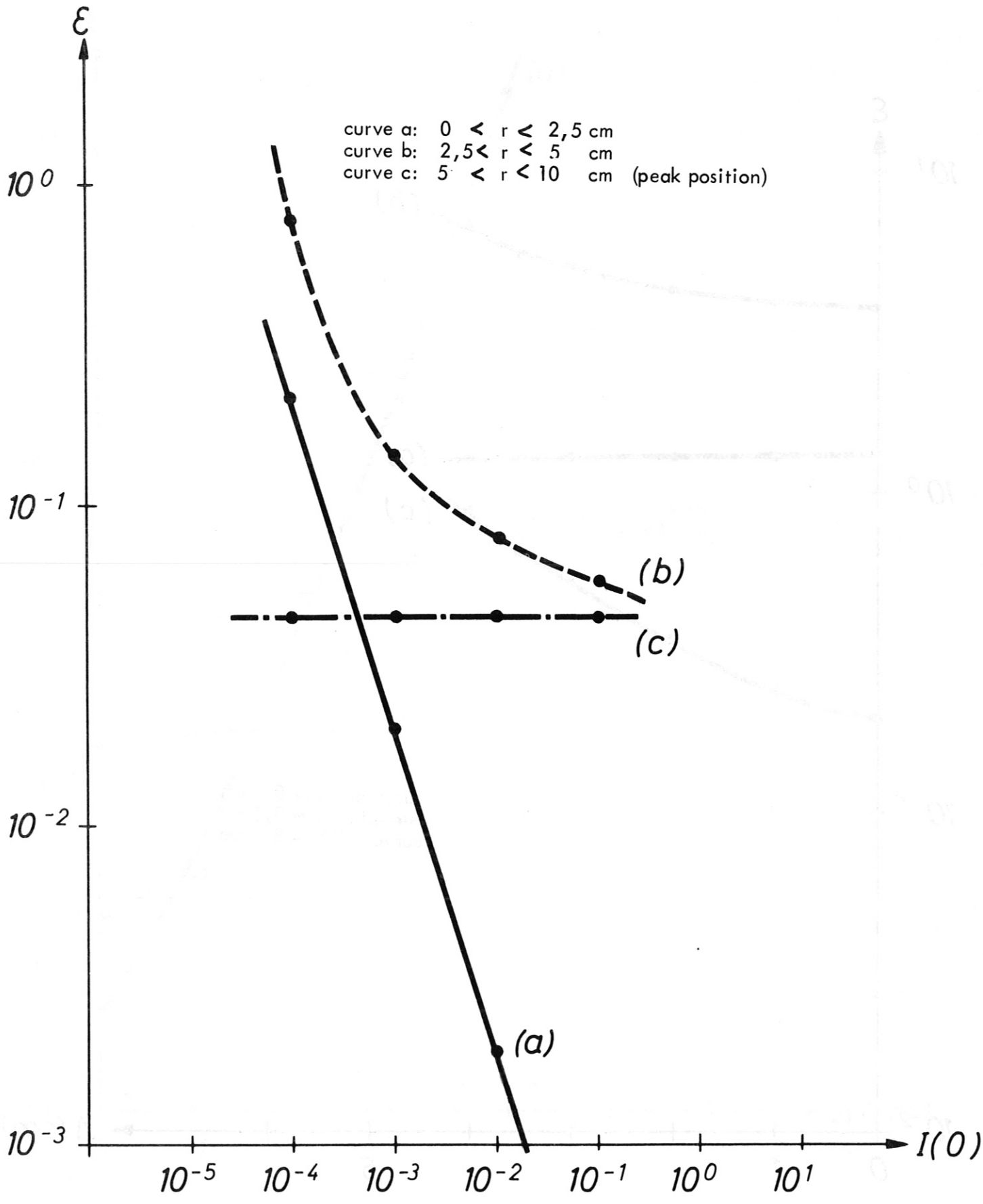

Fig.21 The maximum systematic error ε due to the extended Abel inversion as a function of the central value of the intensity I (o) at different radial positions for ideal spatial resolution. (Compare Fig.18).

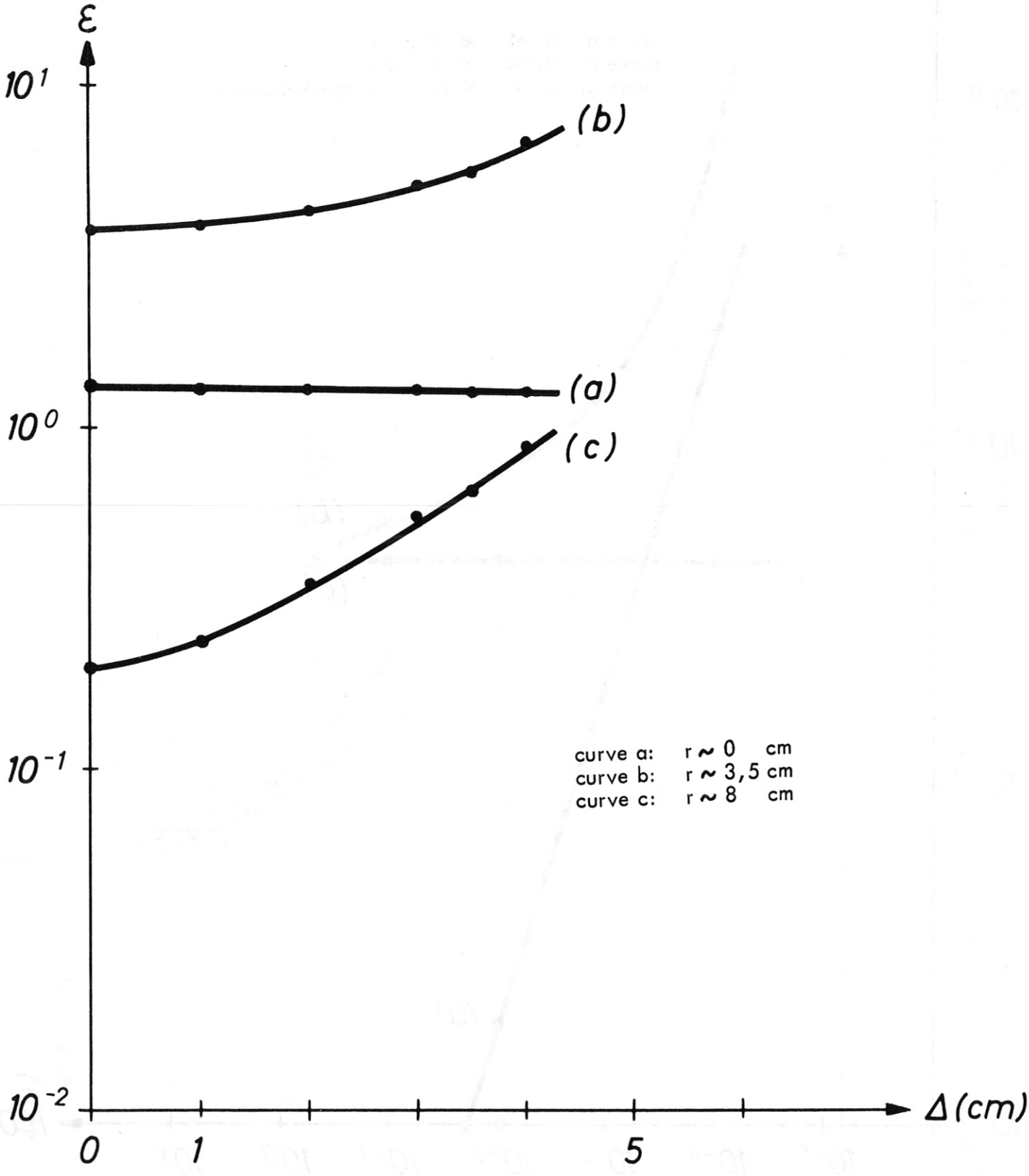

Fig.22 The systematic error ε by Gorenflo-A for various radial positions as a function of the spatial resolution

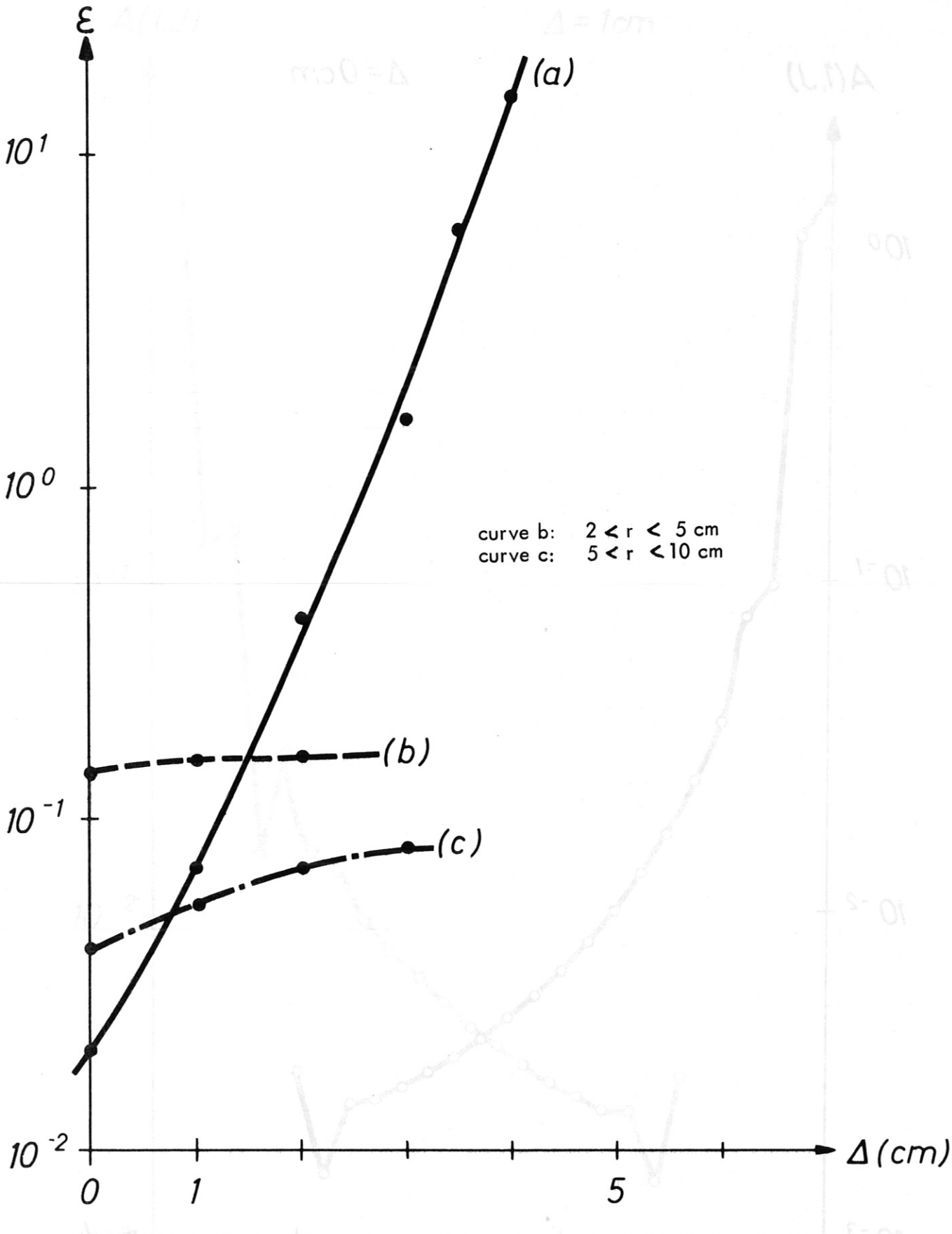

Fig.23 The oscillating error (curve a) and the systematic error (curve b and c) by the extended Abel inversion as a function of the spatial resolution.

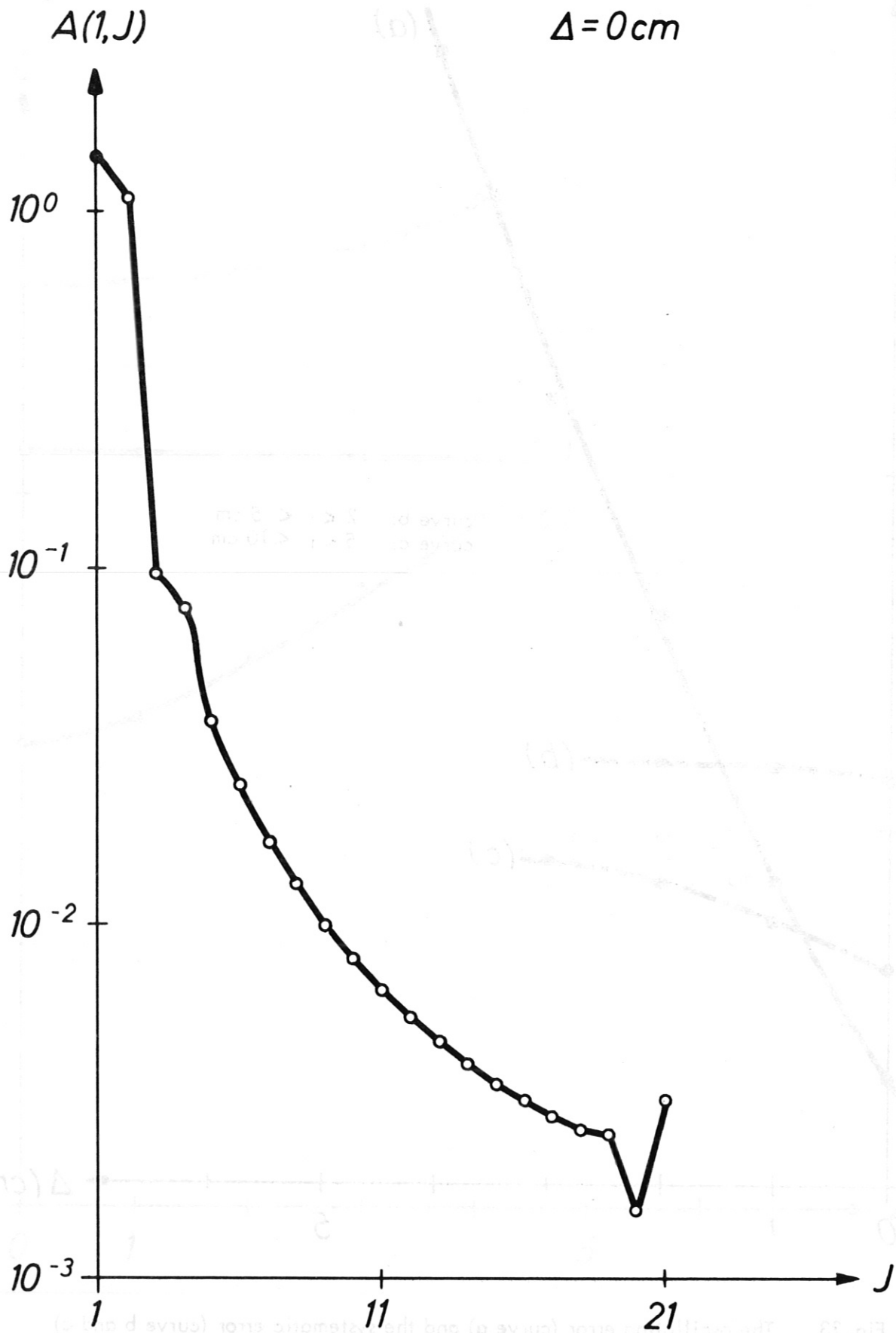

Fig.24

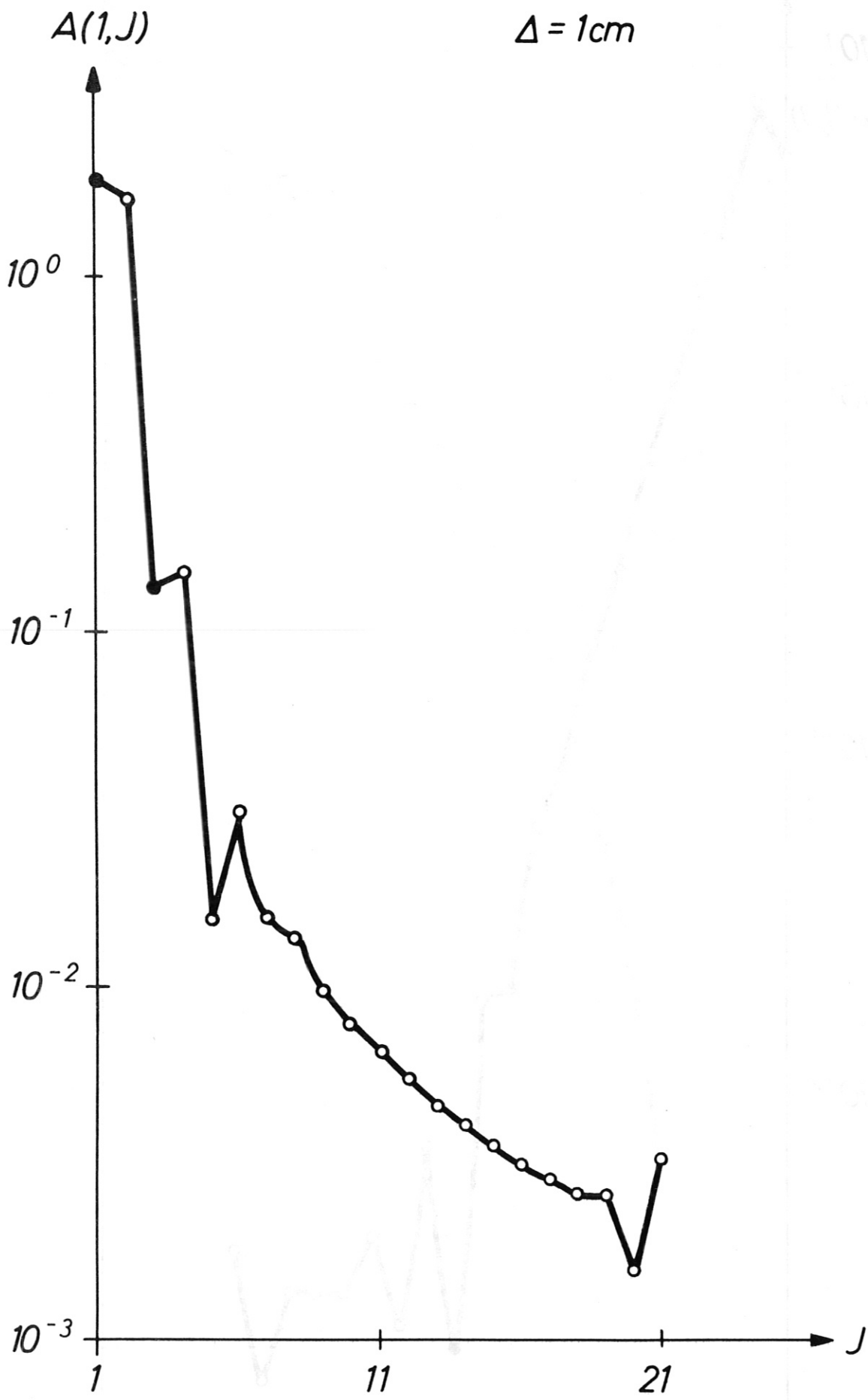

Fig. 25

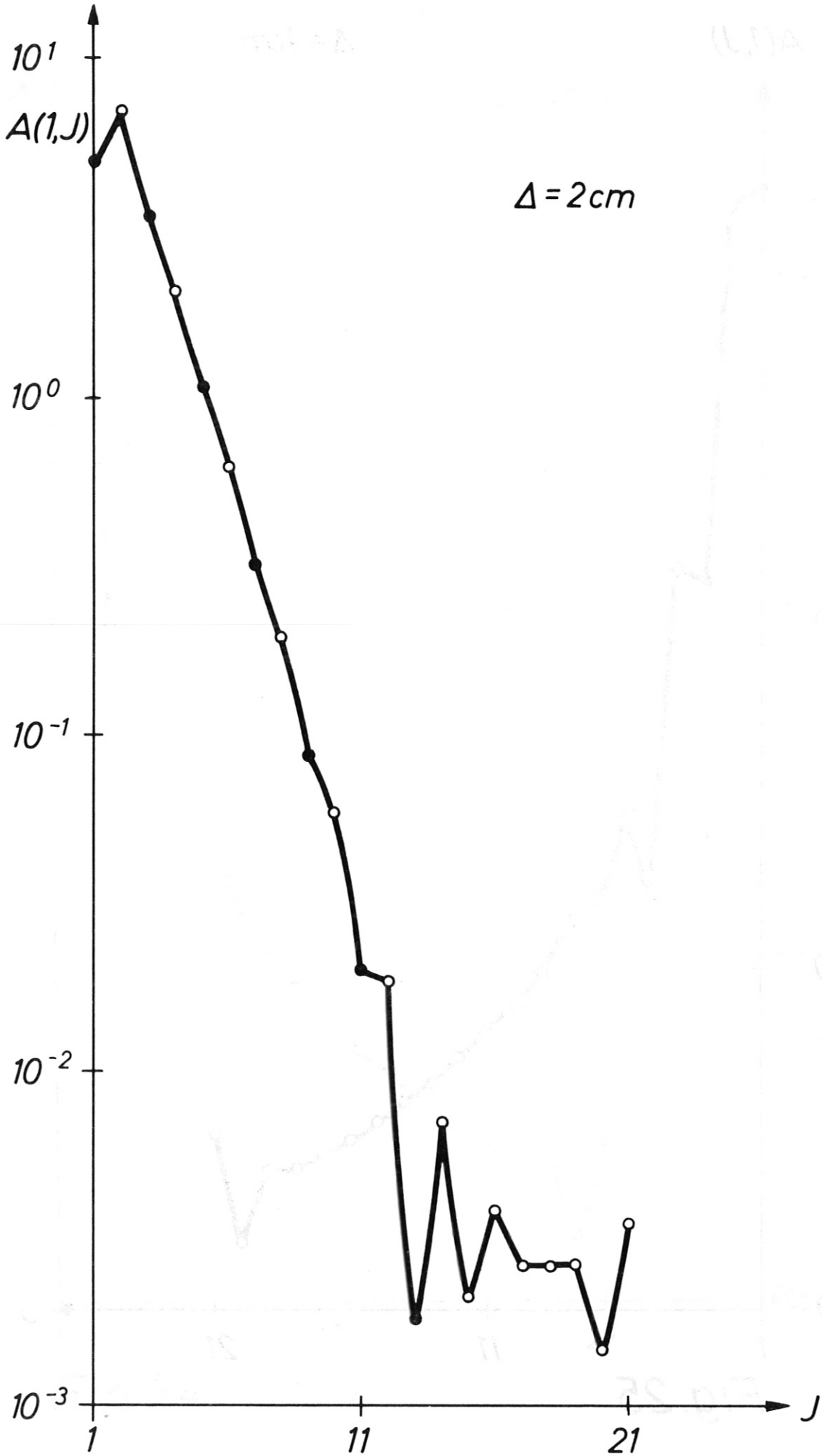

Fig. 26

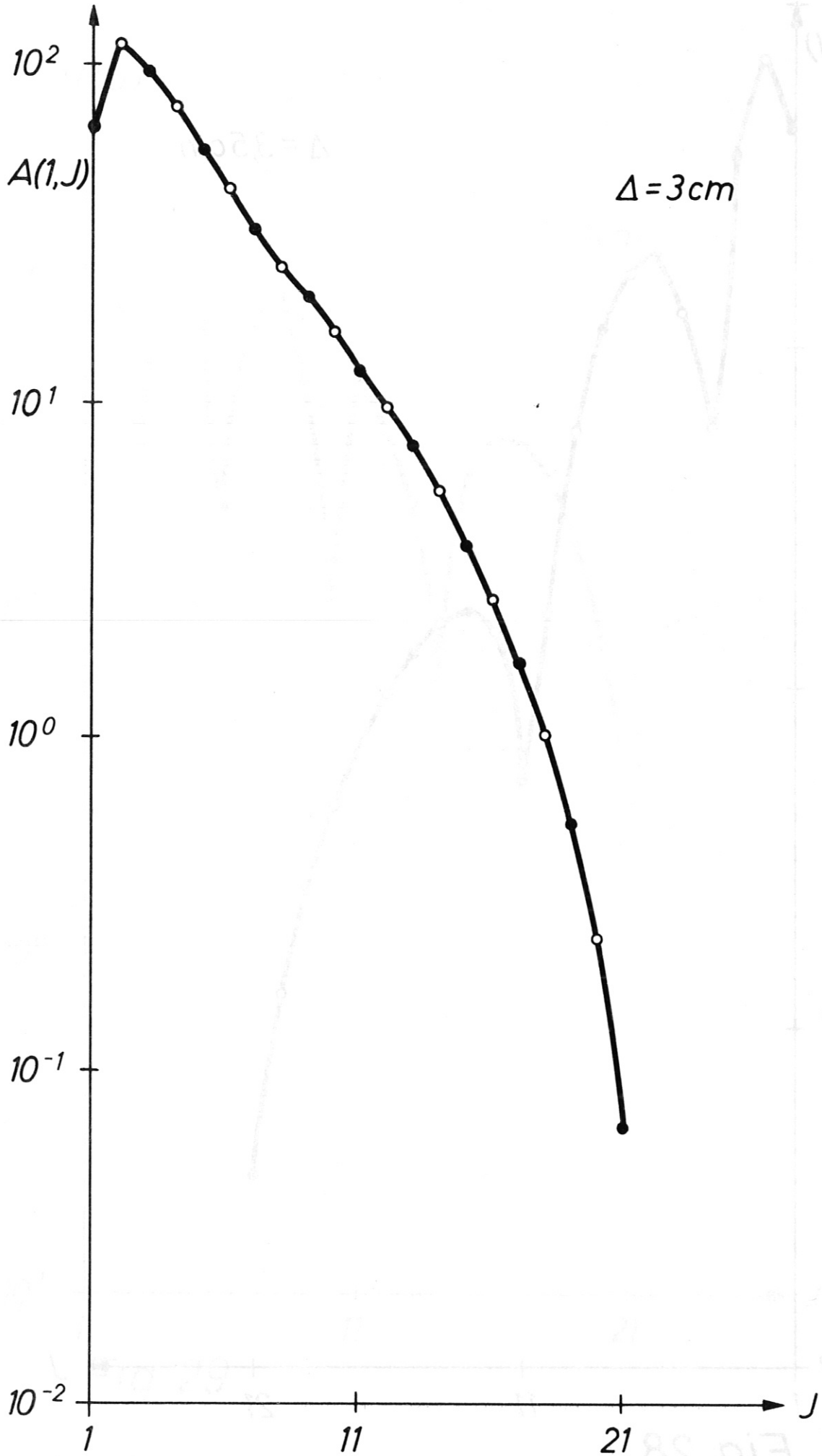

Fig. 27

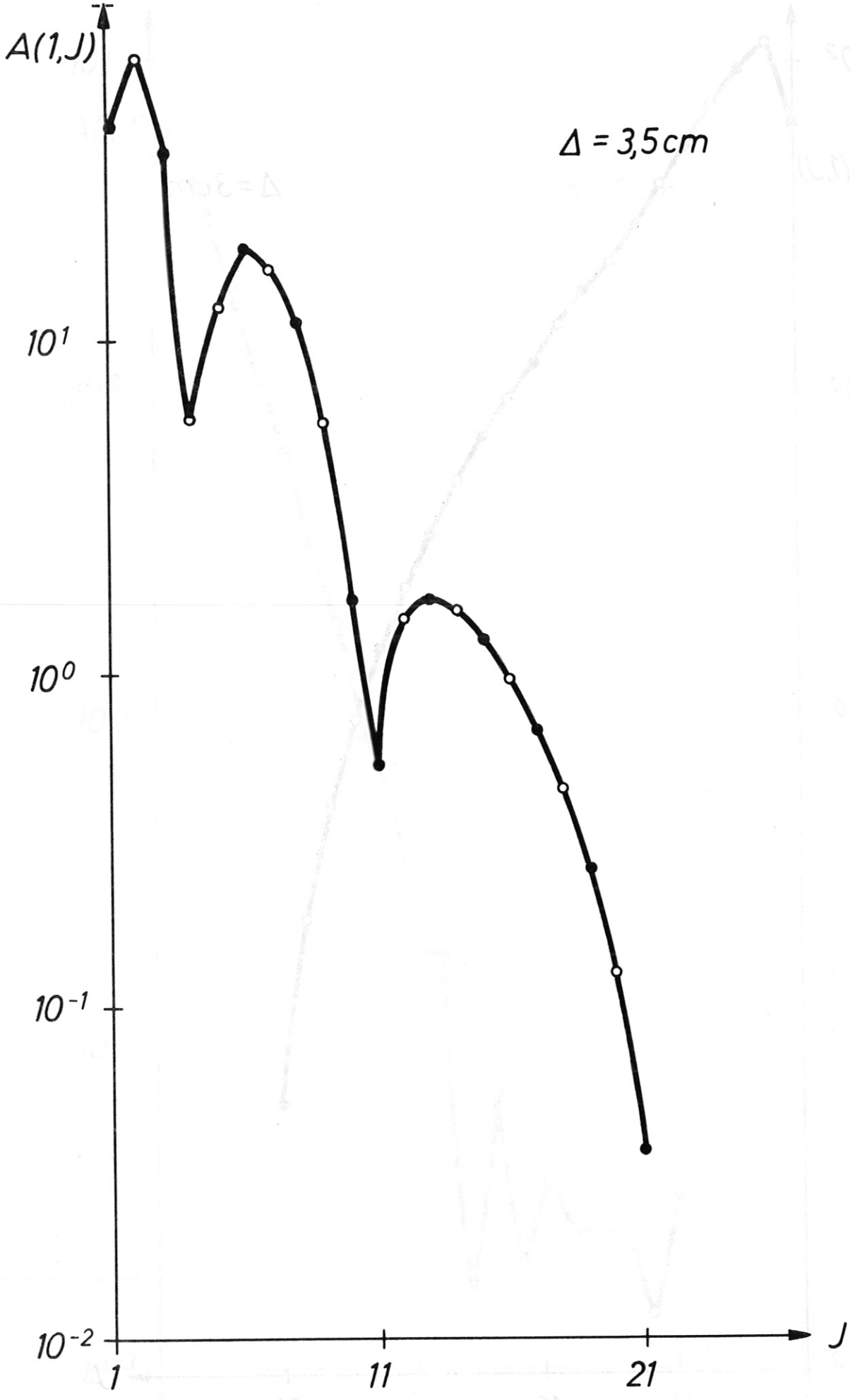

Fig. 28

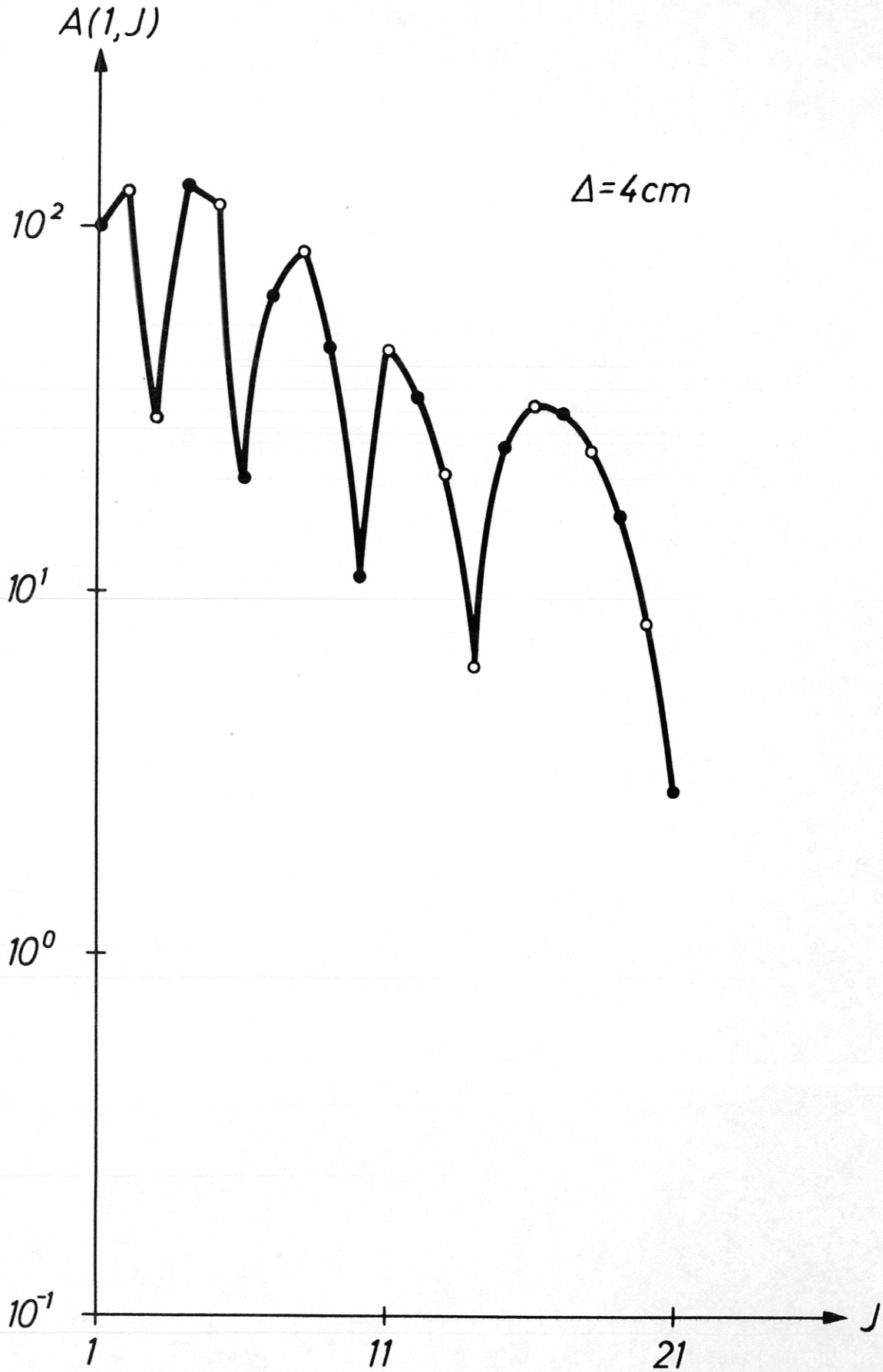

Fig. 29